

# CHEMISTRY

## A European Journal

### Supporting Information

© Copyright Wiley-VCH Verlag GmbH & Co. KGaA, 69451 Weinheim, 2014

#### Dramatic Influence of an Anionic Donor on the Oxygen-Atom Transfer Reactivity of an Mn<sup>V</sup>-Oxo Complex

Heather M. Neu,<sup>[a]</sup> Matthew G. Quesne,<sup>[b]</sup> Tzuhsiu Yang,<sup>[a]</sup> Katharine A. Prokop-Prigge,<sup>[a]</sup> Kyle M. Lancaster,<sup>[c]</sup> James Donohoe,<sup>[c]</sup> Serena DeBeer,<sup>\*[c, d]</sup> Sam P. de Visser,<sup>\*[b]</sup> and David P. Goldberg<sup>\*[a]</sup>

chem\_201404349\_sm\_miscellaneous\_information.pdf

## **Supporting Information**

**Materials.** All reactions were performed under an argon atmosphere using dry solvents and standard Schlenk techniques. The  $(\text{TBP}_8\text{Cz})\text{Mn}^{\text{III}}$  and  $(\text{TBP}_8\text{Cz})\text{Mn}^{\text{V}}(\text{O})$  complexes were synthesized according to published methods.<sup>[1]</sup> Solvents were purified via a Pure-Solv solvent purification system from Innovative Technologies, Inc. Dichloromethane and toluene were distilled under argon over calcium hydride.  $\text{H}_2^{18}\text{O}$  (97%  $^{18}\text{O}$ ) was purchased from Cambridge Isotopes, Inc. All other reagents were purchased from Sigma-Aldrich at the highest level of purity and were used as received.

**Instrumentation.** UV-vis spectroscopy was performed on a Hewlett-Packard 8542 diode-array spectrophotometer equipped with HP Chemstation software. A 400 nm longpass filter was placed directly between the sample quartz cuvette and the spectrophotometer light source to prevent decomposition of the  $[(\text{TBP}_8\text{Cz})\text{Mn}^{\text{V}}(\text{O})(\text{CN})]^-$  complex. The temperature dependent kinetics were performed on a Hewlett Packard 8453 diode-array spectrophotometer, equipped with an Unisoku USP-203A cryostat, using a 1 cm modified Schlenk cuvette. Gas chromatography mass spectrometry (GC-MS) was carried out and recorded using a Hewlett-Packard 6890 series gas chromatograph system, equipped with a 5973N mass selective detector. Laser desorption ionization with a time-of-flight analyzer (LDI-TOF) was conducted on a Bruker Autoflex III TOF/TOF instrument, equipped with a nitrogen laser at 335 nm using an MTP 384 ground steel target plate.

**X-ray Absorption Spectroscopy (XAS) Sample Preparation.** A solution of  $(\text{TBP}_8\text{Cz})\text{Mn}^{\text{V}}(\text{O})$  (10 mM) in benzonitrile (200  $\mu\text{L}$ ) at 25 °C was combined with  $\text{Bu}_4\text{N}^+\text{CN}^-$  (10 or 100 equiv). Samples were loaded into 150 microliter Delrin XAS cells with 38 micron Kapton windows, immediately frozen in liquid nitrogen, and stored at 77 K until XAS measurements were performed.

**X-ray Absorption Spectroscopy Data Collection.** All XAS data were recorded at the Stanford Synchrotron Radiation Laboratory (SSRL) on focused beam line 9-3. A Si(220) monochromator was used for energy selection. A Rh-coated mirror (set to a cutoff of 10 keV) was used for harmonic rejection, in combination with 25% detuning of the monochromator. All data were measured in transmission mode to  $k = 12 \text{ \AA}^{-1}$ , stopping at the Fe K-edge. Internal energy calibration was performed by simultaneous measurement of the absorption of a Mn foil placed between a second and third ionization chamber. The first inflection point of the Mn foil was assigned to 6539.0 eV. Samples were monitored for photoreduction throughout the course of data collection. Only those scans that showed no evidence of photoreduction were used in the final averages. The averaged data were processed as described previously.<sup>[2]</sup> A second-order polynomial was fit to the pre-edge region and subtracted from the entire spectrum. A three-region cubic spline was used to model the background above the edge using the program PySpline.<sup>[3]</sup> Theoretical EXAFS spectra were calculated using FEFF.<sup>[4],[5]</sup> The resulting spectra were fit to the data using EXAFSPAK<sup>[6]</sup> as described previously.<sup>[2]</sup>

**Product Analysis for Thioanisole Oxidation.** In a typical reaction, a stirring solution of  $(\text{TBP}_8\text{Cz})\text{Mn}^{\text{V}}(\text{O})$  (5 mM) in toluene (1 mL) was combined with  $\text{Bu}_4\text{N}^+\text{CN}^-$  (5 mM) at 25 °C. A stock solution of dodecane in toluene (0.1 M) was prepared and 20  $\mu\text{L}$  of the stock solution was added to the reaction as an internal standard. To initiate the reaction, thioanisole (8 M) was added, and isosbestic conversion of  $[(\text{TBP}_8\text{Cz})\text{Mn}^{\text{V}}(\text{O})(\text{CN})]^-$  ( $\lambda_{\text{max}} = 419, 634 \text{ nm}$ ) to  $[(\text{TBP}_8\text{Cz})\text{Mn}^{\text{III}}(\text{CN})]^-$  ( $\lambda_{\text{max}} = 443, 492, 694 \text{ nm}$ ) was observed by sampling of the reaction mixture and analysis by UV-vis spectroscopy. Upon completion of the reaction, the solution was concentrated to ~50  $\mu\text{L}$  under vacuum, and immediately analyzed by GC-FID. The product methyl phenyl sulfoxide, (MPSO) was identified by comparison with an authentic sample. Yields

were obtained by comparing the integration of the product peak with the integration of the internal standard peak and comparison with a dodecane calibration curve. The yield of 84% for MPSO is an average of two runs.

**Preparation of  $[(\text{TBP}_8\text{Cz})\text{Mn}^{\text{V}}(^{18}\text{O})(\text{CN})]^-$  and Reaction with Thioanisole.** Following an earlier report,<sup>[7]</sup> 30  $\mu\text{L}$  of  $\text{H}_2^{18}\text{O}$  was added to a solution of  $(\text{TBP}_8\text{Cz})\text{Mn}^{\text{V}}(\text{O})$  (3 mM) in dry  $\text{CH}_2\text{Cl}_2$  (5 mL). The solution was then stirred vigorously for 48 h to ensure complete exchange of the terminal oxo group with  $\text{H}_2^{18}\text{O}$ . The reaction was analyzed by LDI-MS (LDI-TOF: isotopic cluster centered at  $m/z$  1427.8) and fitting of the isotopic distribution pattern gave an  $^{18}\text{O}$  incorporation of 78%. The  $^{18}\text{O}$  labeled sample was dried under vacuum for 48 h. The solid  $(\text{TBP}_8\text{Cz})\text{Mn}^{\text{V}}(^{18}\text{O})$  was then dissolved in dry toluene (1.6 mL) and  $\text{Bu}_4\text{N}^+\text{CN}^-$  (1 equiv) was added. A mass spectrometry sample was taken out and analyzed by LDI-MS (LDI-TOF: isotopic cluster centered at  $m/z$  1453.4) and fitting of the isotopic distribution pattern gave an  $^{18}\text{O}$  incorporation of 35%. The addition of  $\text{Bu}_4\text{N}^+\text{CN}^-$  likely introduces residual  $\text{H}_2\text{O}$ , accounting for lower  $^{18}\text{O}$  incorporation in the 6-coordinate complex. The OAT reaction was initiated by the addition of excess thioanisole (1.6 M) and progress was monitored by thin layer chromatography (TLC), showing complete conversion of  $[(\text{TBP}_8\text{Cz})\text{Mn}^{\text{V}}(\text{O})(\text{CN})]^-$  ( $R_f = 0.9$ ,  $\text{CH}_2\text{Cl}_2$  neat on silica) to  $[(\text{TBP}_8\text{Cz})\text{Mn}^{\text{III}}(\text{CN})]^-$  ( $R_f = 0.2$ ,  $\text{CH}_2\text{Cl}_2$  neat on silica) after stirring for 19 h. The solution was then concentrated to  $\sim 50 \mu\text{L}$  under vacuum and analyzed directly by GC-MS. Peaks for the labeled and unlabeled product methyl phenyl sulfoxide were observed at  $m/z$  140.2 and 142.2, and their area ratio gave an  $^{18}\text{O}$  incorporation of 71% based on total  $^{18}\text{O}$  label in the starting complex. The  $^{18}\text{O}$  incorporation percentage is an average of two runs.

**Kinetic Measurements.** In a typical reaction, a solution of  $(\text{TBP}_8\text{Cz})\text{Mn}^{\text{V}}(\text{O})$  (11  $\mu\text{M}$ ) in dry toluene (2 mL) was combined with  $\text{Bu}_4\text{N}^+\text{CN}^-$  (11 mM) at 25 °C and excess dibutyl sulfide

(DBS) was added immediately to initiate the reaction. In the absence of substrate, the  $[(\text{TBP}_8\text{Cz})\text{Mn}^{\text{V}}(\text{O})(\text{CN})]^-$  complex decays to  $[(\text{TBP}_8\text{Cz})\text{Mn}^{\text{III}}(\text{CN})]^-$  after  $\sim 25$  min under the same conditions. Thus the concentration of DBS was maintained such that the OAT reactions were completed in 5-15 minutes. The changes in absorbance were monitored by UV-vis spectroscopy, and showed isosbestic decay of  $[(\text{TBP}_8\text{Cz})\text{Mn}^{\text{V}}(\text{O})(\text{CN})]^-$  ( $\lambda_{\text{max}} = 419, 634$  nm) and the formation of  $[(\text{TBP}_8\text{Cz})\text{Mn}^{\text{III}}(\text{CN})]^-$  ( $\lambda_{\text{max}} = 443, 492, 694$  nm). The pseudo-first-order rate constants,  $k_{\text{obs}}$ , were obtained by nonlinear least-squares fitting of plots of the growth in absorbance of  $[(\text{TBP}_8\text{Cz})\text{Mn}^{\text{III}}(\text{CN})]^-$  at (694 nm) or decay of  $[(\text{TBP}_8\text{Cz})\text{Mn}^{\text{V}}(\text{O})(\text{CN})]^-$  (634 nm) versus time to eq. 1:

$$\text{Abs}_t = \text{Abs}_f + (\text{Abs}_0 - \text{Abs}_f)\exp(-k_{\text{obs}}t) \quad \text{Eq. 1}$$

where  $\text{Abs}_f$  = final absorbance,  $\text{Abs}_0$  = initial absorbance and  $\text{Abs}_t$  = absorbance at time (t). Second-order rate constants were obtained from the slope of the best-fit line of the linear plot of  $k_{\text{obs}}$  versus substrate concentration.

**Temperature Dependence of the Rate Constants.** A solution of  $(\text{TBP}_8\text{Cz})\text{Mn}^{\text{V}}(\text{O})$  (13  $\mu\text{M}$ ) in dry toluene (2 mL) was combined with DBS (21 mM), and brought to the desired temperature. The reaction was then initiated by the addition of  $\text{Bu}_4\text{N}^+\text{CN}^-$  (13 mM) and the temperature was maintained at  $\pm 0.1^\circ\text{C}$  throughout the reaction. The changes in absorbance were monitored by UV-vis spectroscopy showing the isosbestic decay of  $[(\text{TBP}_8\text{Cz})\text{Mn}^{\text{V}}(\text{O})(\text{CN})]^-$  ( $\lambda_{\text{max}} = 419, 634$  nm) and formation of  $[(\text{TBP}_8\text{Cz})\text{Mn}^{\text{III}}(\text{CN})]^-$  ( $\lambda_{\text{max}} = 443, 492, 694$  nm). The pseudo-first-order ( $k_{\text{obs}}$ ) rate constants were obtained over a sixty-degree temperature range (40 to -20  $^\circ\text{C}$ ). The pseudo-first-order rate constant at each temperature was divided by the concentration of substrate to yield a second-order rate constant ( $k$ ). Activation parameters were determined from the plot of  $\ln(k/T)$  vs  $1/T$ .

**Computational Methods.** All calculations were performed using the Orca or Gaussian-09 program packages.<sup>[8],[9]</sup>

**TD-DFT Calculations for XAS Pre-edge Transitions.** Optimized geometries of  $^1[(H_8Cz)Mn^V(O)]$  and  $^1[(H_8Cz)Mn^V(O)(CN)]^-$  were obtained using the unrestricted hybrid-GGA UB3LYP<sup>[10]</sup> with dispersion correction (D3).<sup>[11]</sup> A relativistic effective core potential basis set SDD<sup>[12]</sup> was used for Mn, and a split-valence double- $\zeta$  basis set with one set of polarization functions 6-31G(d)<sup>[13]</sup> was used for the remaining atoms. This combination of functional and basis sets has been shown to give good results on transition metal complexes.<sup>[14]</sup> The resolution of identity (RIJ) and the chain-of-sphere (COSX) approximations on the correlation and the exchange interaction, respectively, with auxiliary basis sets of Karlsruhe double- $\zeta$  quality (def2-SVP/J and def2-SVP/C, respectively),<sup>[15]</sup> were used to improve the wall clock time with neglectable error being introduced.<sup>[16]</sup> Single point energy calculations followed by TD-DFT were performed using the optimized geometry according to the literature.<sup>[17]</sup> For the TD-DFT, the unrestricted hybrid-meta-GGA UTPSSh<sup>[18]</sup> functional with the scalar-relativistically recontracted (SARC)<sup>[19]</sup> version of the Karlsruhe basis set def2-TZVP(-f)<sup>[20]</sup> (“def2” version of the triplet- $\zeta$  basis set with one set of the angular momentum deleted) was applied to all atoms. Zero-order regular approximation was applied to recontract the basis set to account for relativistic effects and the integration grid was increased to 4. The RIJCOSX approximation with the decontracted auxiliary basis set def2-TZVP/J<sup>[15]</sup> was applied to Coulomb and exchange correlations of the electrons. Solvent effect was modeled using the conductor-like screening model (COSMO)<sup>[21]</sup> with a dielectric constant of 26.0 and refractive index of 1.528 for benzonitrile. For TD-DFT, the donor core orbital (Mn 1s) was localized and 100 excitations from the donor into the lowest unoccupied orbitals were performed to cover as many transitions as

possible that could have gave rise to the pre-edge feature in the XAS experiment. Transitions through quadrupole moments were included in the calculation. The TammDancoff approximation<sup>[22]</sup> for TD-DFT was applied by default in Orca. The result of the TD-DFT calculations was plotted using orca\_mapspc application using 3 eV Gaussian broadening to facilitate visual comparison to the experiment. An up-shift of 36.3 eV for the calculated spectrum was applied according to the literature<sup>[17]</sup> in order to fit the transition energy of the pre-edge.

**Gaussian Calculations on Spin-state Ordering and Reactivity.** The oxygen-atom transfer reactivity with dimethylsulfide (DMS) as a model substrate and  $[(\text{H}_8\text{Cz})\text{Mn}^{\text{V}}(\text{O})(\text{L})]$  with L = no ligand or  $\text{CN}^-$  was investigated by DFT calculations. We followed procedures as previously applied to manganese corrolazine complexes<sup>[7][23]</sup> that have been well tested and generally reproduce experimental free energies of activation to within 3 – 4 kcal mol<sup>-1</sup>.<sup>[24]</sup> Geometries were optimized in Gaussian-09 using the unrestricted B3LYP<sup>[25]</sup> density functional method in combination with an LACVP basis set on manganese and 6-31G on the rest of the atoms, basis set BS1. An analytical frequency at the same level confirmed the structures as local minima (with real frequencies only) or first-order saddle points with a single imaginary frequency for the correct mode. To improve the quality of the energy calculations, we ran single point calculations on the optimized structures using an LACV3P+ basis set on manganese and 6-311+G\* on the rest of the atoms, basis set BS2. Subsequently, we also did single points at UB3LYP/BS2 using the conductor polarized continuum model in Gaussian with a dielectric constant mimicking toluene to match the experimental kinetics. In addition, we investigated the effects of dispersion on the reaction energies by doing a single point UB3LYP-D3/BS2 calculation using the model of Grimme as implemented in Gaussian.<sup>[11]</sup>

As computational chemistry methods can be sensitive to the choice of the density functional method,<sup>[26]</sup> we did geometry optimizations and calculated spin-state orderings using UB3LYP,<sup>[25]</sup> UBP86<sup>[27]</sup> and M06<sup>[28]</sup> for a selection of structures, see details below. As follows, only minor differences in optimized geometries are observed, although some variation in the spin-state ordering is observed. Because of this variation, it was judged necessary to do a series of supporting *ab initio* multireference calculations, *vide infra*. We also tested the effect of the peripheral substituents on the spin-state ordering, geometries and relative energies by extending our model from  $[(H_8Cz)Mn^V(O)(L)]$  to  $[(Me_8Cz)Mn^V(O)(L)]$  and  $[(MP_8Cz)Mn^V(O)(L)]$  for L = no ligand and  $CN^-$ , Me = methyl, and MP = *p*-methylphenyl. To test the effect of the basis set on the optimized geometries we ran calculations at UB3LYP/BS2 and UB3LYP/BS1. In agreement with previous studies, only minor differences were obtained.<sup>[29]</sup>

**Orca calculations on *ab initio* multiconfiguration (MC) studies of  $^1[(H_8Cz)Mn(O)(CN)]^-$  and  $^3[(H_8Cz)Mn(O)(CN)]$ :** To study the energy ordering of the singlet and triplet spin states of  $[(H_8Cz)Mn(O)(CN)]^-$  complete active space self-consistent field (CASSCF) calculations with different sizes of active space were performed to recover the static correlation of the system. Dynamic correlation of  $[(H_8Cz)Mn(O)(CN)]^-$  was recovered using the *N*-electron valence second-order perturbation theory (NEVPT2) upon the converged MC wavefunctions from CASSCF (CASCI). The geometries of the singlet and triplet spin states were obtained from B3LYP/BS1. The resolution of identity approximation and the chain-of-sphere approximation (RIJCOSX) were applied to the Coulomb and exchange correlation, respectively, with auxiliary basis set corresponding to each atomic basis set throughout the calculations below. The initial guess of the MOs was obtained from DFT calculations using the BP86 density functional and a cc-pVTZ basis set on Mn and cc-pVDZ on the rest of the atoms, and integral grid of “4” and

COSX grid of “4” (notation in Orca) with molecular orbitals and unrestricted Hartree-Fock natural orbitals (UNO) for the singlet and triplet states, respectively. Choices of the active space followed literature precedent with slight modifications.<sup>[30]</sup> CASSCF calculations were performed utilizing the same basis set and grids as for DFT. Two different sizes of active space were obtained: the smaller active space of 10 electrons in 9 orbitals (10,9), which included all five Mn orbitals and four ligand orbitals giving rise to 9 LCAO-MOs,  $d_{xz}$ ,  $d_{yz}$ ,  $d_{xz}^*$ , and  $d_{yz}^*$  from combination of 2 Mn  $d_\pi$  orbitals with 2 O  $p_\pi$  orbitals,  $d_{z2}$  and  $d_{z2}^*$  from Mn  $d_{z2}$  orbital and one of the two  $e_g$ -like LCAO of the first coordination sphere,  $d_{x2-y2}$  and  $d_{x2-y2}^*$  from Mn  $d_{x2-y2}$  orbital and the other  $e_g$ -like LCAO of the first coordination sphere, the  $d_{xy}$  orbital does not have the right symmetry to interact with any ligand-based orbitals of close energy to form any significant MOs so it stayed AO-like; the larger active space of 12 electrons in 11 orbitals (12,11) includes all the orbitals in the smaller set and the HOMO and LUMO of the corrolazine  $\pi$  orbitals, which are of the  $a''$  symmetry. Multireference perturbation theory of the  $N$ -electron valence type (NEVPT2) was applied on top of the converged CASSCF wavefunctions. For NEVPT2 calculations, integral transformation was performed using auxiliary basis set RI. CI vectors were truncated with a thresh of  $1 \times 10^{-10}$  before entering the third order density matrix and  $1 \times 10^{-14}$  before the fourth order density matrix, and each state was canonicalized before entering the perturbation treatment.

## References:

- [1] D. E. Lansky, B. Mandimutsira, B. Ramdhanie, M. Clausen, J. Penner-Hahn, S. A. Zvyagin, J. Telser, J. Krzystek, R. Zhan, Z. Ou, K. M. Kadish, L. Zakharov, A. L. Rheingold, D. P. Goldberg, *Inorg. Chem.* **2005**, *44*, 4485-4498.
- [2] J. B. H. Strautmann, S. DeBeer George, E. Bothe, E. Bill, T. Weyhermuller, A. Stammmer, H. Bogge, T. Glaser, *Inorg. Chem.* **2008**, *47*, 6804-6824.
- [3] A. Tenderholt, B. Hedman, K. O. Hodgson, PySpline: A modern, cross-platform program for the processing of raw averaged XAS edge and EXAFS data. In *X-Ray Absorption Fine Structure-XAFS13*, B. Hedman, P. Painetta, Eds. 2007; Vol. 882, pp 105-107.
- [4] A. L. Ankudinov, J. J. Rehr, *Phys. Rev. B* **1997**, *56*, R1712-R1715.
- [5] J. J. Rehr, J. J. Kas, F. D. Vila, M. P. Prange, K. Jorissen, *Phys. Chem. Chem. Phys.* **2010**, *12*, 5503-5513.
- [6] G. N. George, EXAFSPAK, SSRL, SLAC, Stanford University: Stanford, CA, 2000.
- [7] K. A. Prokop, H. M. Neu, S. P. de Visser, D. P. Goldberg, *J. Am. Chem. Soc.* **2011**, *133*, 15874-15877.
- [8] F. Neese, *Wiley Interdiscip. Rev.: Comput. Mol. Sci.* **2012**, *2*, 73-78.
- [9] Gaussian 09, Revision D.01, M. J. Frisch, G. W. Trucks, H. B. Schlegel, G. E. Scuseria, M. A. Robb, J. R. Cheeseman, G. Scalmani, V. Barone, B. Mennucci, G. A. Petersson, H. Nakatsuji, M. Caricato, X. Li, H. P. Hratchian, A. F. Izmaylov, J. Bloino, G. Zheng, J. L. Sonnenberg, M. Hada, M. Ehara, K. Toyota, R. Fukuda, J. Hasegawa, M. Ishida, T. Nakajima, Y. Honda, O. Kitao, H. Nakai, T. Vreven, J. A. Montgomery, Jr., J. E. Peralta, F. Ogliaro, M. Bearpark, J. J. Heyd, E. Brothers, K. N. Kudin, V. N. Staroverov, R. Kobayashi, J. Normand, K. Raghavachari, A. Rendell, J. C. Burant, S. S. Iyengar, J. Tomasi, M. Cossi, N. Rega, J. M. Millam, M. Klene, J. E. Knox, J. B. Cross, V. Bakken, C. Adamo, J. Jaramillo, R. Gomperts, R. E. Stratmann, O. Yazyev, A. J. Austin, R. Cammi, C. Pomelli, J. W. Ochterski, R. L. Martin, K. Morokuma, V. G. Zakrzewski, G. A. Voth, P. Salvador, J. J. Dannenberg, S. Dapprich, A. D. Daniels, Ö. Farkas, J. B. Foresman, J. V. Ortiz, J. Cioslowski, and D. J. Fox, Gaussian, Inc., Wallingford CT, 2009.
- [10] C. T. Lee, W. T. Yang, R. G. Parr, *Phys. Rev. B* **1988**, *37*, 785-789.
- [11] S. Grimme, J. Antony, S. Ehrlich, H. Krieg, *J. Chem. Phys.* **2010**, *132*.
- [12] M. Dolg, U. Wedig, H. Stoll, H. Preuss, *J. Chem. Phys.* **1987**, *86*, 866-872.
- [13] a) W. J. Hehre, R. Ditchfie, J. A. Pople, *J. Chem. Phys.* **1972**, *56*, 2257; b) P.C. Harihara, J. A. Pople, *Theor Chim Acta* **1973**, *28*, 213-222.
- [14] M. Buhl, H. Kabrede, *J. Chem. Theory Comput.* **2006**, *2*, 1282-1290.
- [15] F. Weigend, *Phys. Chem. Chem. Phys.* **2006**, *8*, 1057-1065.
- [16] R. Izsak, F. Neese, *J. Chem. Phys.* **2011**, *135*.
- [17] V. Krewald, B. Lassalle-Kaiser, T. T. Boron, C. J. Pollock, J. Kern, M. A. Beckwith, V. K. Yachandra, V. L. Pecoraro, J. Yano, F. Neese, S. DeBeer, *Inorg. Chem.* **2013**, *52*, 12904-12914.
- [18] V. N. Staroverov, G. E. Scuseria, J. M. Tao, J. P. Perdew, *J. Chem. Phys.* **2003**, *119*, 12129-12137.
- [19] D. A. Pantazis, X. Y. Chen, C. R. Landis, F. Neese, *J. Chem. Theory Comput.* **2008**, *4*, 908-919.
- [20] F. Weigend, R. Ahlrichs, *Phys. Chem. Chem. Phys.* **2005**, *7*, 3297-3305.
- [21] A. Klamt, G. Schuurmann, *J. Chem. Soc., Perkin Trans. 2* **1993**, 799-805.

- [22] S. Hirata, M. Head-Gordon, *Chem. Phys. Lett.* **1999**, *314*, 291-299.
- [23] K. A. Prokop, S. P. de Visser, D. P. Goldberg, *Angew. Chem. Int. Ed.* **2010**, *49*, 5091-5095.
- [24] A. K. Vardhaman, C. V. Sastri, D. Kumar, S. P. de Visser, *Chem. Commun.* **2011**, *47*, 11044-11046.
- [25] a) A. D. Becke, *J. Chem. Phys.* **1993**, *98*, 5648-5652. b) C. T. Lee, W. T. Yang, R. G. Parr, *Phys. Rev. B* **1988**, *37*, 785-789.
- [26] S. P. de Visser, M. G. Quesne, B. Martin, P. Comba, U. Ryde, *Chem Commun* **2014**, *50*, 262-282.
- [27] a) A. D. Becke, *Phys. Rev. A* **1988**, *38*, 3098-3100.b) J. P. Perdew, *Phys. Rev. B* **1986**, *33*, 8822-8824.
- [28] Y. Zhao, D. G. Truhlar, *Theor. Chem. Acc.* **2008**, *120*, 215-241.
- [29] S. P. de Visser, *J. Am. Chem. Soc.* **2010**, *132*, 1087-1097.
- [30] H. L. Zhao, K. Pierloot, E. H. G. Langner, J. C. Swarts, J. Conradie, A. Ghosh, *Inorg. Chem.* **2012**, *51*, 4002-4006.

**Table S1.** EXAFS fit results.

(TBP <sub>8</sub> Cz)Mn <sup>V</sup> (O)			[(TBP <sub>8</sub> Cz)Mn <sup>V</sup> (O)(CN)] <sup>-</sup>		
	R / Å	$\sigma^2 / \text{\AA}^2$		R / Å	$\sigma^2 / \text{\AA}^2$
1 Mn-O	1.54	0.0032	1 Mn-O	1.53	0.0027
4 Mn-N	1.87	0.0027	4 Mn-N	1.87	0.0074
			1 Mn-C/N	2.21	0.0014
8 MnC/N	2.88	0.0105	8 MnC/N	2.86	0.0043
16 MnC/N	3.00	0.0084	16 MnC/N	3.07	0.0049
6 MnC/N	3.29	0.0012	6 MnC/N	3.27	0.0014
$\Delta E_0$ (eV)	-3.7		$\Delta E_0$ (eV)	-3.6	
Error <sup>[a]</sup>	0.314		Error <sup>[a]</sup>	0.287	

[a] EXAFS error is defined as:  $F = [\sum k^6 (\chi_{\text{exptl}} - \chi_{\text{calcd}})^2 / \sum k^6 \chi_{\text{exptl}}^2]^{1/2}$

**EXAFS Fitting Results.** Table S1 summarizes the best fits for the (TBP<sub>8</sub>Cz)Mn<sup>V</sup>(O) and [(TBP<sub>8</sub>Cz)Mn<sup>V</sup>(O)(CN)]<sup>-</sup> complexes. For (TBP<sub>8</sub>Cz)Mn<sup>V</sup>(O) the error value increases from 0.31 with inclusion of a short Mn-O vector to 0.49 when this vector is not included. Similarly for the [(TBP<sub>8</sub>Cz)Mn<sup>V</sup>(O)(CN)]<sup>-</sup>, exclusion of the short Mn-O increases the fit error from 0.29 to 0.40, providing clear evidence for the presence of a short Mn-O bond in both complexes. Fits were also attempted in which the long 2.21 Å Mn-C/N vector was excluded from the [(TBP<sub>8</sub>Cz)Mn<sup>V</sup>(O)(CN)]<sup>-</sup> fits. These fits resulted in a modest increase in the error from 0.29 to 0.33. We also note that the increase in coordination number is further supported by the increase in outershell scattering (due to coordinated CN) and the decrease in pre-edge intensity (consistent with a more centrosymmetric 6-coordinate environment).

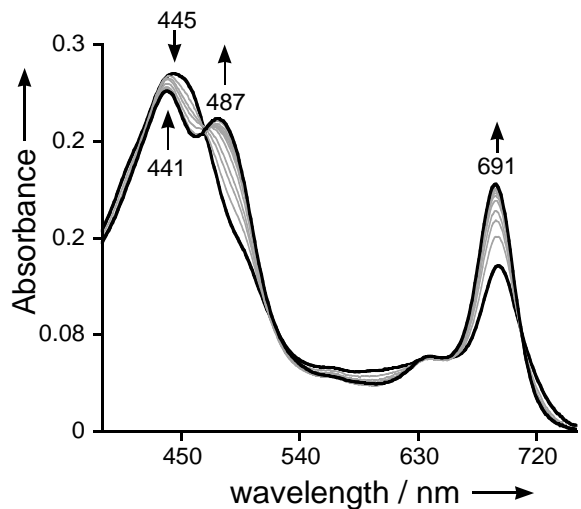


**Figure S1.** UV-vis spectral changes for the reaction of  $(\text{TBP}_8\text{Cz})\text{Mn}^{\text{III}}$  (4.0  $\mu\text{M}$ ) +  $\text{Bu}_4\text{N}^+\text{CN}^-$  (0.1-1.0 equiv) to give  $[(\text{TBP}_8\text{Cz})\text{Mn}^{\text{III}}(\text{CN})]^-$  (441, 487, 691 nm) in toluene at 25  $^\circ\text{C}$ .

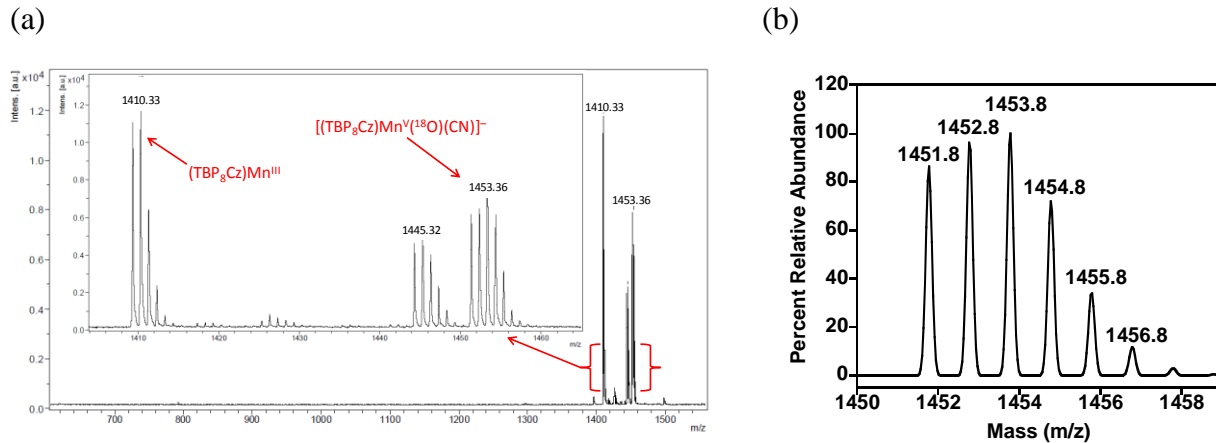


**Figure S2.** (a) LDI-Mass spectrum of  $[(\text{TBP}_8\text{Cz})\text{Mn}^{\text{V}}(^{18}\text{O})(\text{CN})]^-$ . (b) Isotopic distribution for  $[(\text{TBP}_8\text{Cz})\text{Mn}^{\text{V}}(\text{O})(\text{CN})]^-$  showing  $^{18}\text{O}$  incorporation of 35%.

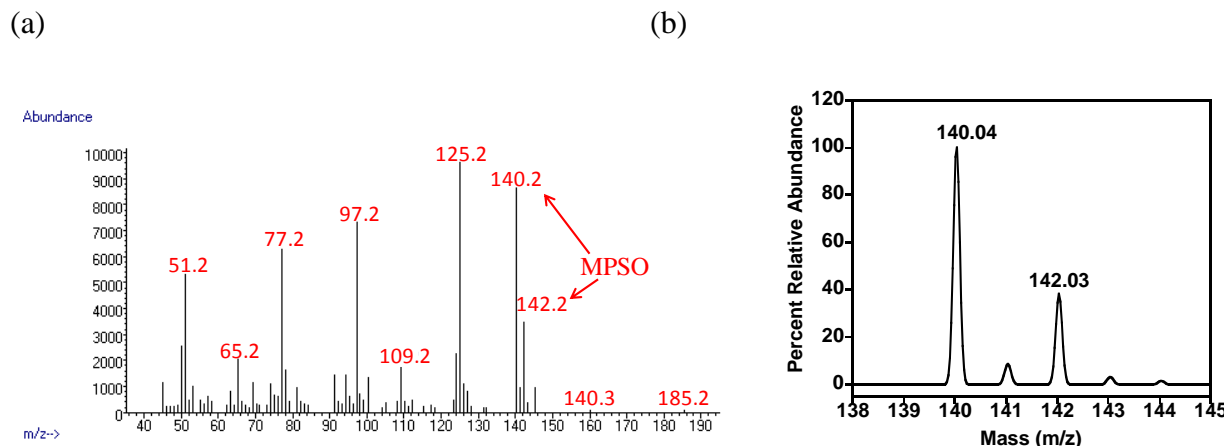
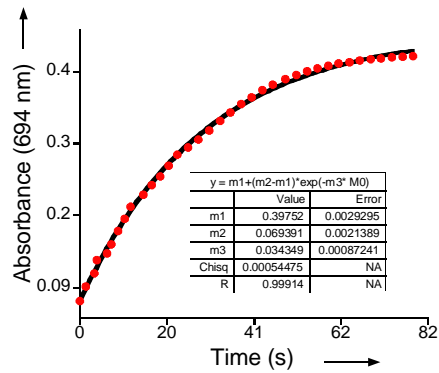
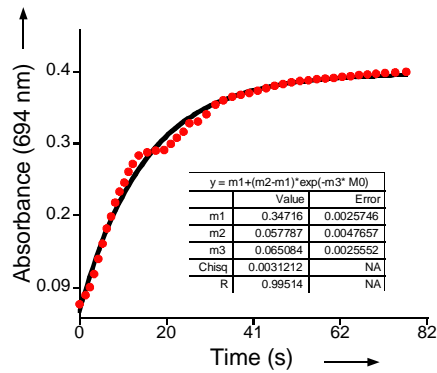


**Figure S3.** (a) GC-MS for the methyl phenyl sulfoxide product from the OAT reaction of  $[(\text{TBP}_8\text{Cz})\text{Mn}^{\text{V}}(\text{O})(\text{CN})]^-$  ( $^{18}\text{O}$  35%) with thioanisole as the substrate. (b) Isotopic distribution of methyl phenyl sulfoxide showing  $^{18}\text{O}$  incorporation of 25%.

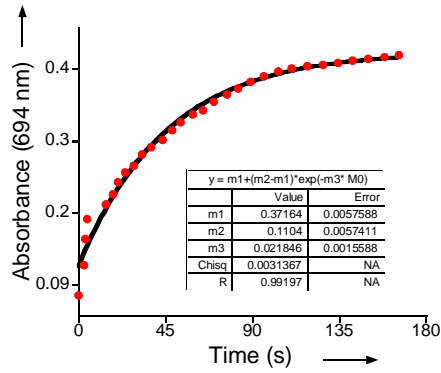
1)



2)



3)



4)

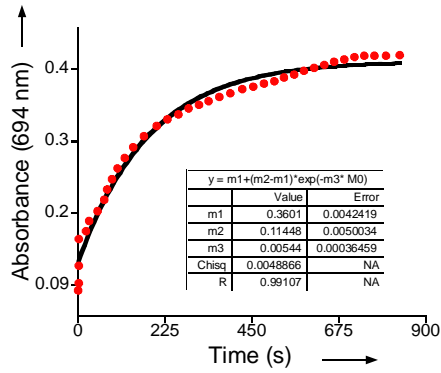


**Figure S4.** Changes in absorbance versus time for the growth of  $[(\text{TBP}_8\text{Cz})\text{Mn}^{\text{III}}(\text{CN})]^-$  (694 nm) during the reaction of  $[(\text{TBP}_8\text{Cz})\text{Mn}^{\text{V}}(\text{O})(\text{CN})]^-$  with  $[\text{DBS}] = 1)$  5.7 mM, 2) 8.6 mM, 3) 3.4 mM, and 4) 2.0 mM. Red circles = experimental data, solid black line = best fit.

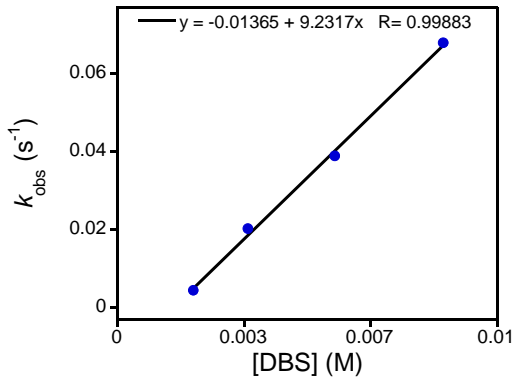


**Figure S5.** Plot of  $k_{obs}$  versus concentration of DBS with best fit line.

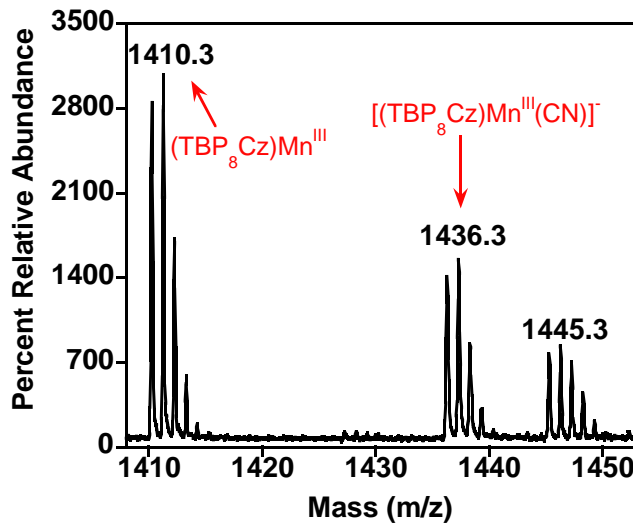


**Figure S6.** LDI-Mass spectrum of the completed reaction mixture for the reaction of  $[(TBP_8Cz)Mn^V(O)(CN)]^-$  with DBS (5.7 mM).

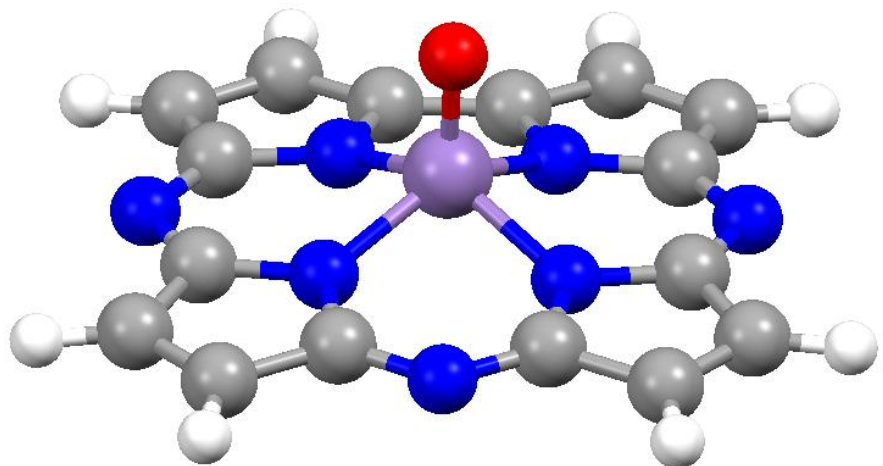


**Fig S7.** Optimized geometry for  ${}^1[(\text{H}_8\text{Cz})\text{Mn}^{\text{V}}(\text{O})]$  using RIJCOSX-B3LYP-D3/SDD/6-31G(d).

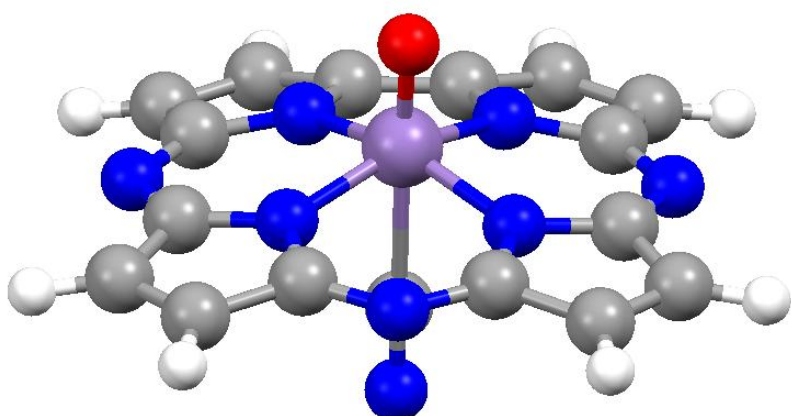


**Fig S8.** Optimized geometry for  ${}^1[(\text{H}_8\text{Cz})\text{Mn}^{\text{V}}(\text{O})(\text{CN})]^-$  using RIJCOSX-B3LYP-D3/SDD/6-31G(d).

**Table S2.** Selected molecular parameters from optimized geometries of singlet  $(H_8Cz)Mn^V(O)$  and  $[(H_8Cz)Mn^V(O)(CN)]^-$  using Orca with RIJCOSX-B3LYP-D3/SDD/6-31G(d). Distances shown in Å.

	Mn-O	Mn-L	Mn-N <sub>av</sub>	$\Delta_{Mn}$
$[(H_8Cz)Mn^V(O)]$	1.519		1.884	0.659
$[(H_8Cz)Mn^V(O)(CN)]^-$	1.548	2.192	1.896	0.525

**Table S3.** Spin densities from optimized geometries of singlet  $(H_8Cz)Mn^V(O)$  and  $[(H_8Cz)Mn^V(O)(CN)]^-$  using Orca with RIJCOSX-B3LYP-D3/SDD/6-31G(d).

Singlet spin states:	$\rho(Mn)$	$\rho(O)$	$\rho(Cz)$	$\rho(L)$
$[(H_8Cz)Mn^V(O)]$	0.00	0.00	0.00	
$[(H_8Cz)Mn^V(O)(CN)]^-$	0.00	0.00	0.00	0.00

**Table S4.** Fragment charges from optimized geometries of singlet  $(H_8Cz)Mn^V(O)$  and  $[(H_8Cz)Mn^V(O)(CN)]^-$  using Orca with RIJCOSX-B3LYP-D3/SDD/6-31G(d).

Singlet spin states:	$Q(Mn)$	$Q(O)$	$Q(Cz)$	$Q(L)$
$[(H_8Cz)Mn^V(O)]$	1.14	-0.37	-0.77	
$[(H_8Cz)Mn^V(O)(CN)]^-$	0.42	-0.39	-0.89	-0.13

**Table S5.** Comparison between selected molecular parameters from EXAFS of  $(TBP_8Cz)Mn^V(O)$  and  $[(TBP_8Cz)Mn^V(O)(CN)]^-$  versus those from optimized geometries of singlet  $(H_8Cz)Mn^V(O)$  and  $[(H_8Cz)Mn^V(O)(CN)]^-$  using Orca with RIJCOSX-B3LYP-D3/SDD/6-31G(d).

	(Cz)Mn <sup>V</sup> (O)		[(Cz)Mn <sup>V</sup> (O)(CN)] <sup>-</sup>	
	EXAFS	DFT	EXAFS	DFT
Mn-O (Å)	1.54	1.519	1.53	1.548
Mn-N (Å)	1.87	1.884	1.87	1.896
Mn-C/N (Å)			2.21	2.192

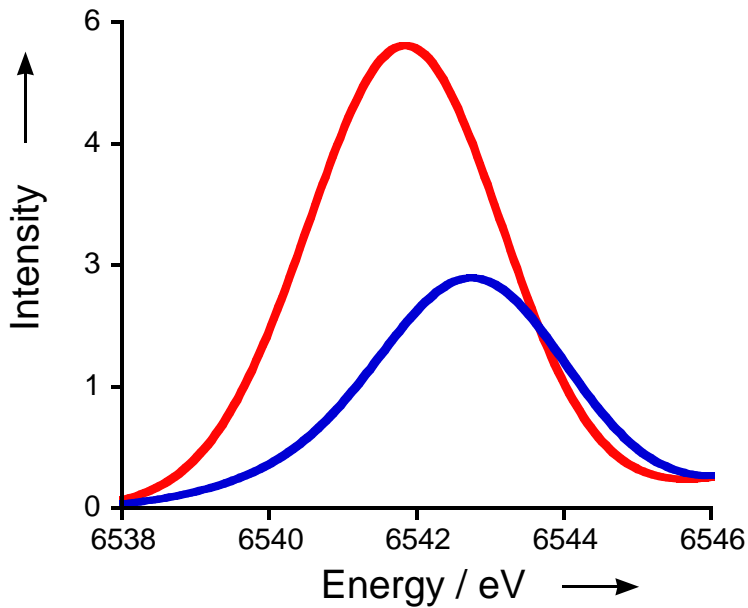


**Fig S9.** Calculated pre-edge absorption bands (TD-DFT) for  ${}^1[(\text{H}_8\text{Cz})\text{Mn}^{\text{V}}(\text{O})]$  (blue) and  ${}^1[(\text{H}_8\text{Cz})\text{Mn}^{\text{V}}(\text{O})(\text{CN})]^-$  (red). The intensity does not reflect the normalized intensity from the experiment. The excitation energies are shifted to higher energy by 36.3 eV according to literature.<sup>[17]</sup>

**Table S6.** Optimized geometries of peripherally substituted manganese(V)-oxo corrolazines with MePh = *p*-methylphenyl, Me = methyl or H for systems without axial ligand or with CN<sup>-</sup> as axial ligand. Data obtained through a full geometry optimization in Gaussian-09 with either B3LYP, BP86 or M06 methods in combination with basis set BS1.

Singlet spin states:	B3LYP:				BP86:				M06:			
	Mn-O	Mn-L	Mn-N <sub>av</sub>	Δ <sub>Mn</sub>	Mn-O	Mn-L	Mn-N <sub>av</sub>	Δ <sub>Mn</sub>	Mn-O	Mn-L	Mn-N <sub>av</sub>	Δ <sub>Mn</sub>
[((MePh) <sub>8</sub> Cz)Mn <sup>V</sup> (O)(CN)] <sup>-</sup>	1.579	2.158	1.894	0.316	1.605	2.150	1.897	0.319	1.571	2.149	1.882	0.323
[((MePh) <sub>8</sub> Cz)Mn <sup>V</sup> (O)]	1.554		1.884	0.544	1.577		1.888	0.526	1.544		1.869	0.529
[((Me <sub>8</sub> Cz)Mn <sup>V</sup> (O)(CN)] <sup>-</sup>	1.577	2.176	1.890	0.327	1.601	2.166	1.892	0.327	1.569	2.160	1.880	0.332
[((Me <sub>8</sub> Cz)Mn <sup>V</sup> (O)]	1.553		1.882	0.570	1.575		1.885	0.563	1.554		1.881	0.564
[((H <sub>8</sub> Cz)Mn <sup>V</sup> (O)(CN)] <sup>-</sup>	1.576	2.168	1.889	0.328	1.598	2.173	1.891	0.332	1.570	2.106	1.886	0.333
[((H <sub>8</sub> Cz)Mn <sup>V</sup> (O)]	1.550		1.883	0.569	1.570		1.887	0.566	1.539		1.871	0.561

Triplet spin states:	B3LYP:				BP86:				M06:			
	Mn-O	Mn-L	Mn-N <sub>av</sub>	Δ <sub>Mn</sub>	Mn-O	Mn-L	Mn-N <sub>av</sub>	Δ <sub>Mn</sub>	Mn-O	Mn-L	Mn-N <sub>av</sub>	Δ <sub>Mn</sub>
[((MePh) <sub>8</sub> Cz)Mn <sup>V</sup> (O)(CN)] <sup>-</sup>	1.813	2.049	1.893	0.035	1.668	2.088	1.906	0.265	1.819	2.043	1.885	0.158
[((MePh) <sub>8</sub> Cz)Mn <sup>V</sup> (O)]	1.623		1.896	0.257	1.621		1.900	0.493	1.634		1.886	0.490
[((Me <sub>8</sub> Cz)Mn <sup>V</sup> (O)(CN)] <sup>-</sup>	1.821	2.057	1.886	0.011	1.670	2.090	1.900	0.251	1.818	2.052	1.881	0.167
[((Me <sub>8</sub> Cz)Mn <sup>V</sup> (O)]	1.621		1.891	0.320	1.622		1.893	0.501	1.643		1.880	0.491
[((H <sub>8</sub> Cz)Mn <sup>V</sup> (O)(CN)] <sup>-</sup>	1.824	2.051	1.885	0.023	1.670	2.080	1.898	0.243	1.815	2.048	1.881	0.163
[((H <sub>8</sub> Cz)Mn <sup>V</sup> (O)]	1.633		1.889	0.483	1.620		1.892	0.497	1.646		1.880	0.483

**Table S7.** Group spin densities and charges of peripherally substituted manganese(V)-oxo corrolazines with MePh = *p*-methylphenyl, Me = methyl or H for systems without axial ligand or with CN<sup>-</sup> as axial ligand. Data obtained with B3LYP.

(a) *Spin densities*

triplet	$\rho(\text{Mn})$	$\rho(\text{O})$	$\rho(\text{Cz})$	$\rho(\text{L})$
$[(\text{MePh}_8\text{Cz})\text{Mn}^{\text{V}}(\text{O})(\text{CN})]^-$	2.83	-0.86	0.06	-0.03
$[(\text{MePh}_8\text{Cz})\text{Mn}^{\text{V}}(\text{O})]$	2.21	-0.19	-0.02	-
$[(\text{Me}_8\text{Cz})\text{Mn}^{\text{V}}(\text{O})(\text{CN})]^-$	2.84	-0.88	0.07	-0.03
$[(\text{Me}_8\text{Cz})\text{Mn}^{\text{V}}(\text{O})]$	2.19	-0.20	0.01	-
$[(\text{H}_8\text{Cz})\text{Mn}^{\text{V}}(\text{O})(\text{CN})]^-$	2.86	-0.88	0.06	-0.03
$[(\text{H}_8\text{Cz})\text{Mn}^{\text{V}}(\text{O})]$	2.30	-0.32	0.02	-

(b) *Charges*

triplet	$Q(\text{Mn})$	$Q(\text{O})$	$Q(\text{Cz})$	$Q(\text{L})$
$[(\text{MePh}_8\text{Cz})\text{Mn}^{\text{V}}(\text{O})(\text{CN})]^-$	0.73	-0.28	-1.15	-0.31
$[(\text{MePh}_8\text{Cz})\text{Mn}^{\text{V}}(\text{O})]$	1.07	-0.32	-0.75	-
$[(\text{Me}_8\text{Cz})\text{Mn}^{\text{V}}(\text{O})(\text{CN})]^-$	0.71	-0.29	-1.10	-0.32
$[(\text{Me}_8\text{Cz})\text{Mn}^{\text{V}}(\text{O})]$	1.07	-0.32	-0.75	-
$[(\text{H}_8\text{Cz})\text{Mn}^{\text{V}}(\text{O})(\text{CN})]^-$	0.71	-0.28	-1.11	-0.32
$[(\text{H}_8\text{Cz})\text{Mn}^{\text{V}}(\text{O})]$	1.07	-0.30	1.23	-

**Table S8.** Absolute (in au) and relative (in kcal mol<sup>-1</sup>) energies of manganese(V)-oxo complexes in the singlet and triplet spin states with different corrolazine description.

**B3LYP Results.**

	BS1 E [au]	BS1 ZPE [au]	BS2 E [au]
<b>Singlet:</b>			
[(MePh <sub>8</sub> Cz)Mn <sup>V</sup> (O)(CN)]	-3431.991984	1.107094	-3433.555524
[(MePh <sub>8</sub> Cz)Mn <sup>V</sup> (O)]	-3339.144932	1.100991	-3340.645461
[(Me <sub>8</sub> Cz)Mn <sup>V</sup> (O)(CN)]	-1583.959692	0.456008	-1584.739108
[(Me <sub>8</sub> Cz)Mn <sup>V</sup> (O)]	-1491.125212	0.450230	-1491.840698
[(H <sub>8</sub> Cz)Mn <sup>V</sup> (O)(CN)]	-1269.478113	0.233621	-1270.127637
[(H <sub>8</sub> Cz)Mn <sup>V</sup> (O)]	-1176.635009	0.227895	-1177.220228
<b>Triplet:</b>			
[(MePh <sub>8</sub> Cz)Mn <sup>V</sup> (O)(CN)]	-3431.978888	1.104349	-3433.550095
[(MePh <sub>8</sub> Cz)Mn <sup>V</sup> (O)]	-3339.133523	1.099398	-3340.637066
[(Me <sub>8</sub> Cz)Mn <sup>V</sup> (O)(CN)]	-1583.946834	0.453118	-1584.732102
[(Me <sub>8</sub> Cz)Mn <sup>V</sup> (O)]	-1491.111615	0.448233	-1491.830838
[(H <sub>8</sub> Cz)Mn <sup>V</sup> (O)(CN)]	-1269.489329	0.231695	-1270.088264
[(H <sub>8</sub> Cz)Mn <sup>V</sup> (O)]	-1176.616592	0.225426	-1177.194338

	ΔE	ΔE+ZPE	ΔE	ΔE+ZPE
<b>Singlet:</b>				
BS1	BS1	BS1	BS2	BS2
[(MePh <sub>8</sub> Cz)Mn <sup>V</sup> (O)(CN)]	0.00	0.00	0.00	0.00
[(MePh <sub>8</sub> Cz)Mn <sup>V</sup> (O)]	0.00	0.00	0.00	0.00
[(Me <sub>8</sub> Cz)Mn <sup>V</sup> (O)(CN)]	0.00	0.00	0.00	0.00
[(Me <sub>8</sub> Cz)Mn <sup>V</sup> (O)]	0.00	0.00	0.00	0.00
[(H <sub>8</sub> Cz)Mn <sup>V</sup> (O)(CN)]	0.00	0.00	0.00	0.00
[(H <sub>8</sub> Cz)Mn <sup>V</sup> (O)]	0.00	0.00	0.00	0.00
<b>Triplet:</b>				
[(MePh <sub>8</sub> Cz)Mn <sup>V</sup> (O)(CN)]	8.22	6.50	3.41	1.68
[(MePh <sub>8</sub> Cz)Mn <sup>V</sup> (O)]	7.16	6.16	5.27	4.27
[(Me <sub>8</sub> Cz)Mn <sup>V</sup> (O)(CN)]	8.07	6.26	4.40	2.58
[(Me <sub>8</sub> Cz)Mn <sup>V</sup> (O)]	8.53	7.28	6.19	4.93
[(H <sub>8</sub> Cz)Mn <sup>V</sup> (O)(CN)]	-7.04	-8.25	24.71	23.50
[(H <sub>8</sub> Cz)Mn <sup>V</sup> (O)]	11.56	10.01	16.25	14.70

**Table S9.** Absolute (in au) and relative (in kcal mol<sup>-1</sup>) energies of manganese(V)-oxo complexes in the singlet and triplet spin states with different corrolazine description.

**BP86 Results.**

	BS1 E [au]	BS1 ZPE [au]	BS2 E [au]
<b>Singlet:</b>			
[(MePh <sub>8</sub> Cz)Mn <sup>V</sup> (O)(CN)]	-3432.205535	1.073675	-3433.674967
[(MePh <sub>8</sub> Cz)Mn <sup>V</sup> (O)]	-3339.349251	1.068811	-3340.757608
[(Me <sub>8</sub> Cz)Mn <sup>V</sup> (O)(CN)]	-1584.162377	0.455067	-1584.899341
[(Me <sub>8</sub> Cz)Mn <sup>V</sup> (O)]	-1491.121155	0.449191	-1491.995081
[(H <sub>8</sub> Cz)Mn <sup>V</sup> (O)(CN)]	-1269.690348	0.226027	-1270.306915
[(H <sub>8</sub> Cz)Mn <sup>V</sup> (O)]	-1176.837502	0.225441	-1177.393190
<b>Triplet:</b>			
[(MePh <sub>8</sub> Cz)Mn <sup>V</sup> (O)(CN)]	-3432.191417	1.072777	-3433.667770
[(MePh <sub>8</sub> Cz)Mn <sup>V</sup> (O)]	-3339.326321	1.067101	-3340.740549
[(Me <sub>8</sub> Cz)Mn <sup>V</sup> (O)(CN)]	-1584.150247	0.441479	-1584.889769
[(Me <sub>8</sub> Cz)Mn <sup>V</sup> (O)]	-1491.125080	0.434974	-1491.972654
[(H <sub>8</sub> Cz)Mn <sup>V</sup> (O)(CN)]	-1269.679262	0.225026	-1270.297099
[(H <sub>8</sub> Cz)Mn <sup>V</sup> (O)]	-1176.795971	0.218743	-1177.382711

	ΔE	ΔE+ZPE	ΔE	ΔE+ZPE
Singlet:	BS1	BS1	BS2	BS2
[(MePh <sub>8</sub> Cz)Mn <sup>V</sup> (O)(CN)]	0.00	0.00	0.00	0.00
[(MePh <sub>8</sub> Cz)Mn <sup>V</sup> (O)]	0.00	0.00	0.00	0.00
[(Me <sub>8</sub> Cz)Mn <sup>V</sup> (O)(CN)]	0.00	0.00	0.00	0.00
[(Me <sub>8</sub> Cz)Mn <sup>V</sup> (O)]	0.00	0.00	0.00	0.00
[(H <sub>8</sub> Cz)Mn <sup>V</sup> (O)(CN)]	0.00	0.00	0.00	0.00
[(H <sub>8</sub> Cz)Mn <sup>V</sup> (O)]	0.00	0.00	0.00	0.00
<b>Triplet:</b>				
[(MePh <sub>8</sub> Cz)Mn <sup>V</sup> (O)(CN)]	8.86	8.30	4.52	3.95
[(MePh <sub>8</sub> Cz)Mn <sup>V</sup> (O)]	14.39	13.32	10.71	9.63
[(Me <sub>8</sub> Cz)Mn <sup>V</sup> (O)(CN)]	7.61	-0.91	6.01	-2.52
[(Me <sub>8</sub> Cz)Mn <sup>V</sup> (O)]	-2.46	-11.38	14.07	5.15
[(H <sub>8</sub> Cz)Mn <sup>V</sup> (O)(CN)]	6.96	6.33	6.16	5.53
[(H <sub>8</sub> Cz)Mn <sup>V</sup> (O)]	26.06	21.86	6.58	2.37

**Table S10.** Absolute (in au) and relative (in kcal mol<sup>-1</sup>) energies of manganese(V)-oxo complexes in the singlet and triplet spin states with different corrolazine description.

**M06 Results.**

	BS1 E [au]	BS1 ZPE [au]	BS2 E [au]
<b>Singlet:</b>			
[(MePh <sub>8</sub> Cz)Mn <sup>V</sup> (O)(CN)]	-3429.624538	1.105786	-3431.079827
[(MePh <sub>8</sub> Cz)Mn <sup>V</sup> (O)]	-3336.829484	1.099020	-3338.223232
[(Me <sub>8</sub> Cz)Mn <sup>V</sup> (O)(CN)]	-1583.957214	0.458342	-1583.696190
[(Me <sub>8</sub> Cz)Mn <sup>V</sup> (O)]	-1491.125181	0.450416	-1490.850984
[(H <sub>8</sub> Cz)Mn <sup>V</sup> (O)(CN)]	-1268.728049	0.234077	-1269.338981
[(H <sub>8</sub> Cz)Mn <sup>V</sup> (O)]	-1175.935321	0.228259	-1176.484848
<b>Triplet:</b>			
[(MePh <sub>8</sub> Cz)Mn <sup>V</sup> (O)(CN)]	-3429.657681	1.101811	-3431.094108
[(MePh <sub>8</sub> Cz)Mn <sup>V</sup> (O)]	-3336.815024	1.095606	-3338.205183
[(Me <sub>8</sub> Cz)Mn <sup>V</sup> (O)(CN)]	-1582.948193	0.453414	-1583.709349
[(Me <sub>8</sub> Cz)Mn <sup>V</sup> (O)]	-1490.162898	0.446456	-1490.836738
[(H <sub>8</sub> Cz)Mn <sup>V</sup> (O)(CN)]	-1268.748190	0.231534	-1269.350973
[(H <sub>8</sub> Cz)Mn <sup>V</sup> (O)]	-1175.911628	0.224969	-1176.470582

	ΔE	ΔE+ZPE	ΔE	ΔE+ZPE
	BS1	BS1	BS2	BS2
<b>Singlet:</b>				
[(MePh <sub>8</sub> Cz)Mn <sup>V</sup> (O)(CN)]	0.00	0.00	0.00	0.00
[(MePh <sub>8</sub> Cz)Mn <sup>V</sup> (O)]	0.00	0.00	0.00	0.00
[(Me <sub>8</sub> Cz)Mn <sup>V</sup> (O)(CN)]	0.00	0.00	0.00	0.00
[(Me <sub>8</sub> Cz)Mn <sup>V</sup> (O)]	0.00	0.00	0.00	0.00
[(H <sub>8</sub> Cz)Mn <sup>V</sup> (O)(CN)]	0.00	0.00	0.00	0.00
[(H <sub>8</sub> Cz)Mn <sup>V</sup> (O)]	0.00	0.00	0.00	0.00
<b>Triplet:</b>				
[(MePh <sub>8</sub> Cz)Mn <sup>V</sup> (O)(CN)]	-8.14	-10.64	-8.96	-11.46
[(MePh <sub>8</sub> Cz)Mn <sup>V</sup> (O)]	9.07	6.93	11.33	9.18
[(Me <sub>8</sub> Cz)Mn <sup>V</sup> (O)(CN)]	15.18	12.08	-8.26	-11.35
[(Me <sub>8</sub> Cz)Mn <sup>V</sup> (O)]	16.79	14.31	8.94	6.45
[(H <sub>8</sub> Cz)Mn <sup>V</sup> (O)(CN)]	-12.64	-14.23	-7.53	-9.12
[(H <sub>8</sub> Cz)Mn <sup>V</sup> (O)]	14.87	12.80	8.95	6.89

**Table S11.** Absolute energies along the reaction mechanism of DMS sulfoxidation by  $[(\text{H}_8\text{Cz})\text{Mn}(\text{O})\text{CN}]^-$  as obtained with Gaussian-09.

	From UB3LYP/BS1 freq:		BS2//BS1
	E [au]	ZPE [au]	E [au]
$^1[\text{Mn}^{\text{V}}(\text{O})(\text{Cz})\text{CN}]^-$	-1269.478148	0.233601	-1270.131529
$^1\text{RC}_{\text{CN}}$	-1747.455612	0.311231	-1748.193316
$^1\text{TS}_{\text{SO,CN}}$	-1747.423017	0.309701	-1748.167815
$^1\text{P}_{\text{CN}}$	-1747.431900	0.310220	-1748.199134

**Table S12.** Relative energies along the reaction mechanism of DMS sulfoxidation by  $[(\text{H}_8\text{Cz})\text{Mn}(\text{O})\text{CN}]^-$  as obtained with Gaussian-09 in the gas-phase.

	$\Delta E$	$\Delta E + \text{ZPE}$	$\Delta E$	$\Delta E + \text{ZPE}$
	[BS1]	[BS1]	[BS2]	[BS2]
$^1\text{RC}_{\text{CN}}$	-5.72	-5.07	-4.05	-3.39
$^1\text{TS}_{\text{SO,CN}}$	14.73	14.43	11.95	11.65
$^1\text{P}_{\text{CN}}$	9.16	9.18	-7.70	-7.68

**Table S13.** Group spin densities and charges of optimized geometries (UB3LYP/BS1) along the sulfoxidation mechanism of DMS by  $[(\text{H}_8\text{Cz})\text{Mn}(\text{O})(\text{CN})]^-$ .

Spin densities:	$\rho_{\text{Mn}}$	$\rho_{\text{O}}$	$\rho_{\text{Cz}}$	$\rho_{\text{L}}$	$\rho_{\text{DMS}}$
$^1[\text{Mn}^{\text{V}}(\text{O})(\text{Cz})\text{CN}]^-$	0.00	0.00	0.00	0.00	
$^1\text{RC}_{\text{CN}}$	0.00	0.00	0.00	0.00	0.00
$^1\text{TS}_{\text{SO,CN}}$	0.04	-0.01	-0.01	-0.01	-0.01
$^1\text{P}_{\text{CN}}$	0.00	-0.01	0.00	0.00	0.00

Charges:	$Q_{\text{Mn}}$	$Q_{\text{O}}$	$Q_{\text{Cz}}$	$Q_{\text{L}}$	$Q_{\text{DMS}}$
$^1[\text{Mn}^{\text{V}}(\text{O})(\text{Cz})\text{CN}]^-$	0.47	-0.27	-0.98	-0.21	
$^1\text{RC}_{\text{CN}}$	0.48	-0.30	-0.96	-0.20	-0.02
$^1\text{TS}_{\text{SO,CN}}$	0.58	-0.47	-1.36	-0.28	0.53
$^1\text{P}_{\text{CN}}$	0.67	-0.60	-1.48	-0.36	0.78

**Table S14.** Group spin densities and charges of single point UB3LYP/BS2 on UB3LYP/BS1 optimized geometries along the mechanism of DMS sulfoxidation by  ${}^1[(\text{H}_8\text{Cz})\text{Mn}(\text{O})(\text{CN})]^-$ .

Spin densities:	$\rho_{\text{Mn}}$	$\rho_{\text{O}}$	$\rho_{\text{Cz}}$	$\rho_{\text{L}}$	$\rho_{\text{DMS}}$
${}^1[\text{Mn}^{\text{V}}(\text{O})(\text{Cz})\text{CN}]^-$	0.00	0.00	0.00	0.00	
${}^1\mathbf{RC}_{\text{CN}}$	0.00	0.00	0.00	0.00	0.00
${}^1\mathbf{TS}_{\text{SO,CN}}$	0.00	0.00	-0.02	0.01	0.01
${}^1\mathbf{P}_{\text{CN}}$	0.00	-0.01	0.01	0.00	0.00

Charges:	$Q_{\text{Mn}}$	$Q_{\text{O}}$	$Q_{\text{Cz}}$	$Q_{\text{L}}$	$Q_{\text{DMS}}$
${}^1[\text{Mn}^{\text{V}}(\text{O})(\text{Cz})\text{CN}]^-$	-2.33	0.02	3.45	-2.14	
${}^1\mathbf{RC}_{\text{CN}}$	-3.20	0.10	4.37	-2.20	-0.07
${}^1\mathbf{TS}_{\text{SO,CN}}$	-1.10	0.03	0.09	-0.41	0.39
${}^1\mathbf{P}_{\text{CN}}$	-0.31	-0.01	-0.56	-0.60	0.48

**Table S15.** Absolute energies along the reaction mechanism of DMS sulfoxidation by  $[(\text{H}_8\text{Cz})\text{Mn}(\text{O})]$  as obtained with Gaussian-09 as obtained with B3LYP.

	E [au]	ZPE [au]	E [au]
$[\text{Mn}^{\text{V}}(\text{O})(\text{Cz})]$	-1176.635104	0.227955	-1177.224190
${}^1\mathbf{RC}_{\text{NL}}$	-1654.604826	0.304846	-1655.281048
${}^1\mathbf{TS}_{\text{SO,NL}}$	-1654.562834	0.302900	-1655.250474
${}^1\mathbf{P}_{\text{NL}}$	-1654.562751	0.303678	-1655.259882

**Table S16.** Relative energies along the reaction mechanism of DMS sulfoxidation by  $[(\text{H}_8\text{Cz})\text{Mn}(\text{O})]$  as obtained with Gaussian-09 as obtained with B3LYP in the gas phase.

	$\Delta E$	$\Delta E+\text{ZPE}$	$\Delta E$	$\Delta E+\text{ZPE}$
	[BS1]	[BS1]	[BS2]	[BS2]
${}^1\mathbf{RC}_{\text{NL}}$	-0.87	-0.67	-0.96	-0.76
${}^1\mathbf{TS}_{\text{SO,NL}}$	25.48	24.46	18.23	17.20
${}^1\mathbf{P}_{\text{NL}}$	25.54	25.00	12.33	11.79

**Table S17.** Relative energies (in kcal mol<sup>-1</sup>) along the reaction mechanism of DMS sulfoxidation by either  $[(\text{H}_8\text{Cz})\text{Mn}(\text{O})]$  or  $[(\text{H}_8\text{Cz})\text{Mn}(\text{O})(\text{CN})]^-$  as obtained in Gaussian after a single point in solvent with a toluene dielectric constant.

	$\Delta E_s+\text{ZPE}$
	[BS2]
${}^1\mathbf{RC}_{\text{CN}}$	-0.3
${}^1\mathbf{TS}_{\text{SO,CN}}$	10.1
${}^1\mathbf{P}_{\text{CN}}$	-9.7
${}^1\mathbf{RC}_{\text{NL}}$	-0.7
${}^1\mathbf{TS}_{\text{SO,NL}}$	21.1
${}^1\mathbf{P}_{\text{NL}}$	15.3

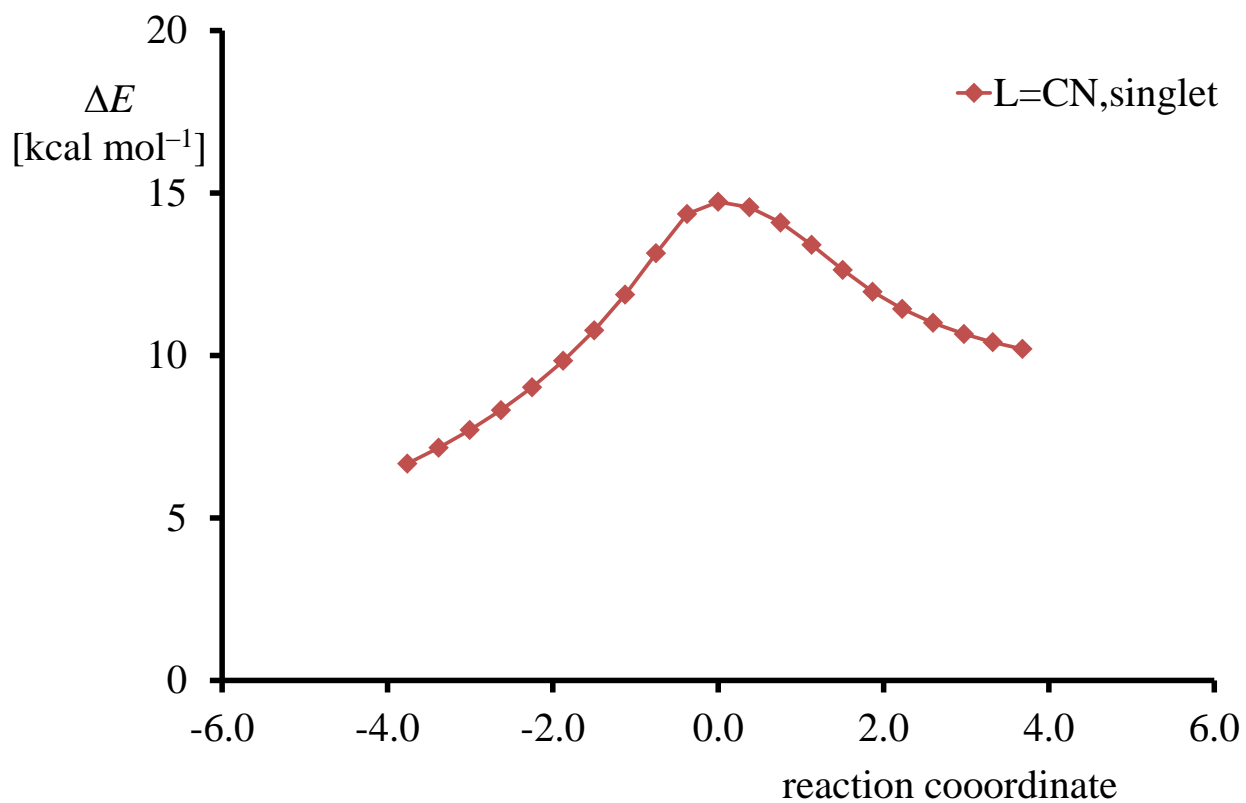


**Figure S10.** IRC scan starting from  ${}^1\text{TS}_{\text{SO,CN}}$  as calculated at UB3LYP/BS1 in Gaussian. The reaction starts on the left-hand-side with reactants and proceeds via the TS to a radical intermediate. Energies are calculated in kcal/mol.

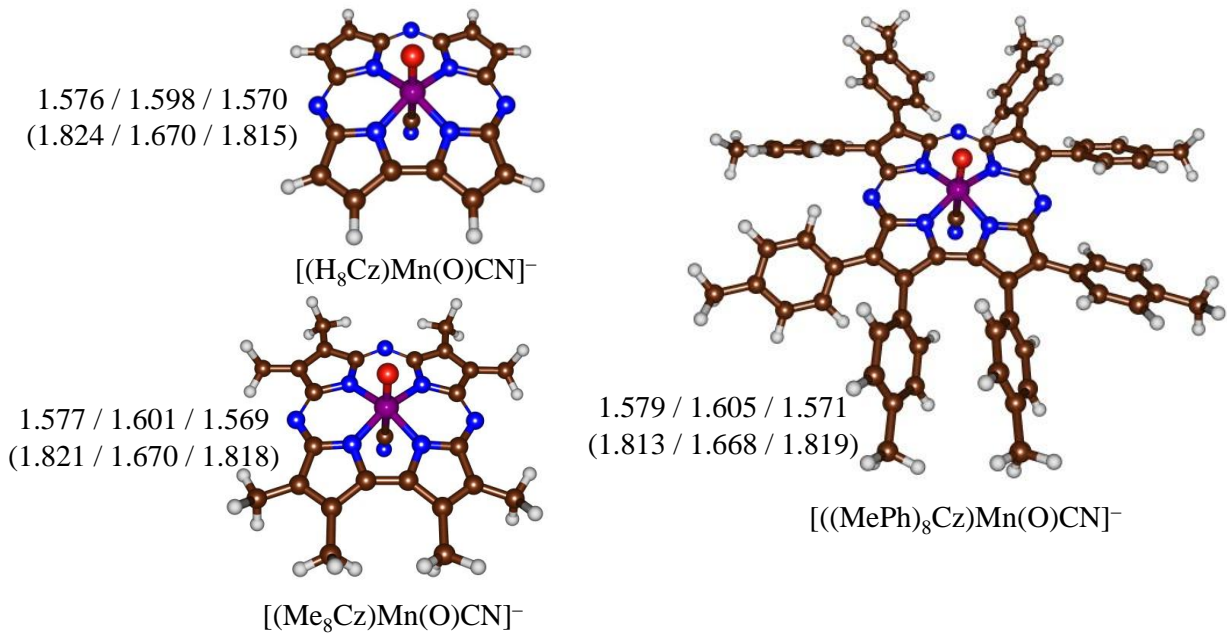


**Figure S11.** Optimized geometries of  ${}^{1,3}[(\text{R}_8\text{Cz})\text{Mn}^{\text{V}}(\text{O})\text{CN}]^-$  with  $\text{R} = \text{H}$ ,  $\text{Me}$  or  $\text{MePh}$  with bond lengths in angstroms ( ${}^3[(\text{R}_8\text{Cz})\text{Mn}^{\text{V}}(\text{O})\text{CN}]^-$  lengths in parentheses). The three sets of data represent B3LYP, BP86 and M06 optimized geometries.

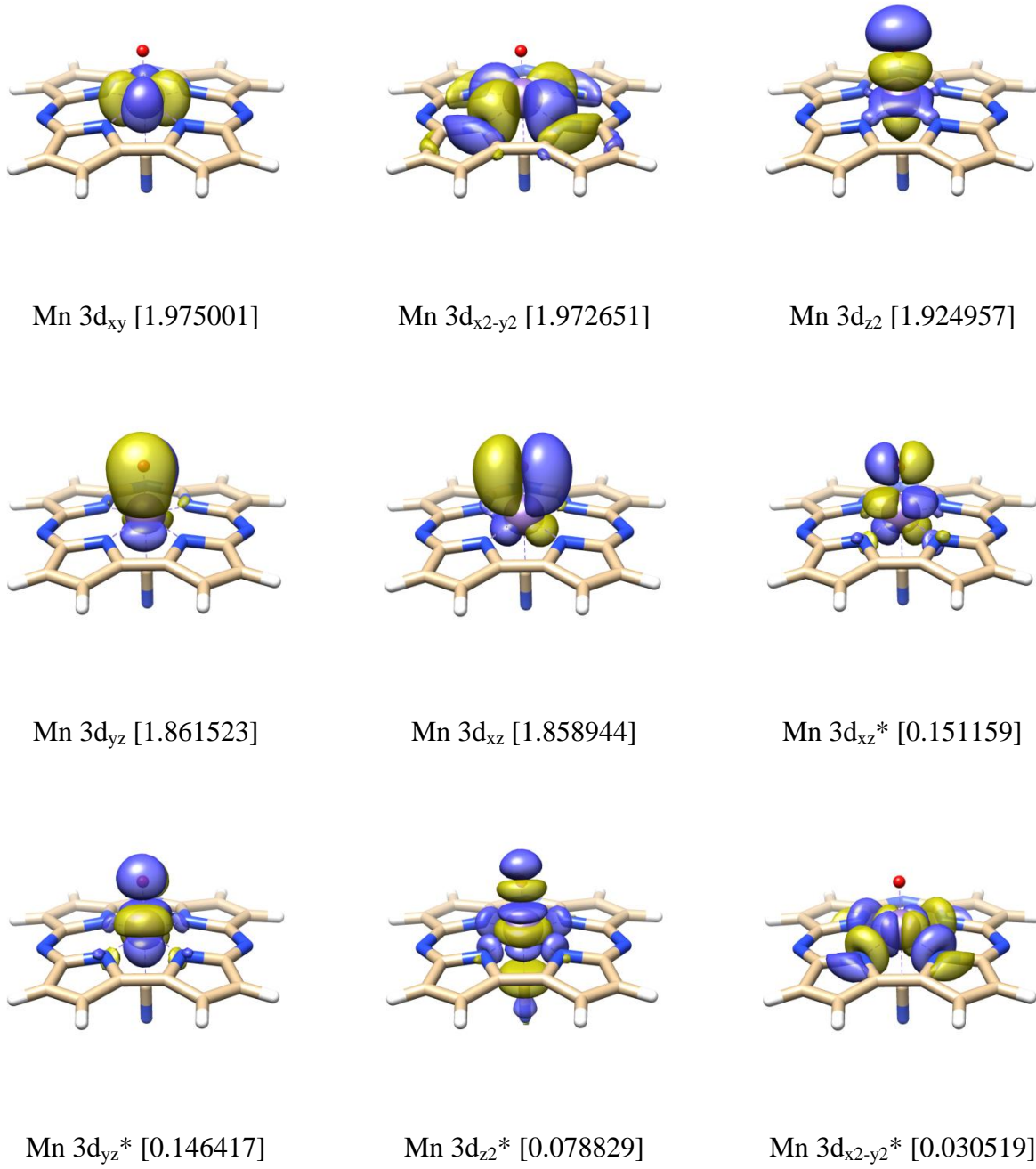


**Figure S12.** Active natural orbitals of  ${}^1[({\text{H}}_8{\text{Cz}}){\text{Mn}}(\text{O})(\text{CN})]^-$  from RIJCOSX-CASSCF(10,9)/cc-pVTZ/cc-pVDZ. The opposite phases are shown in either blue or yellow.

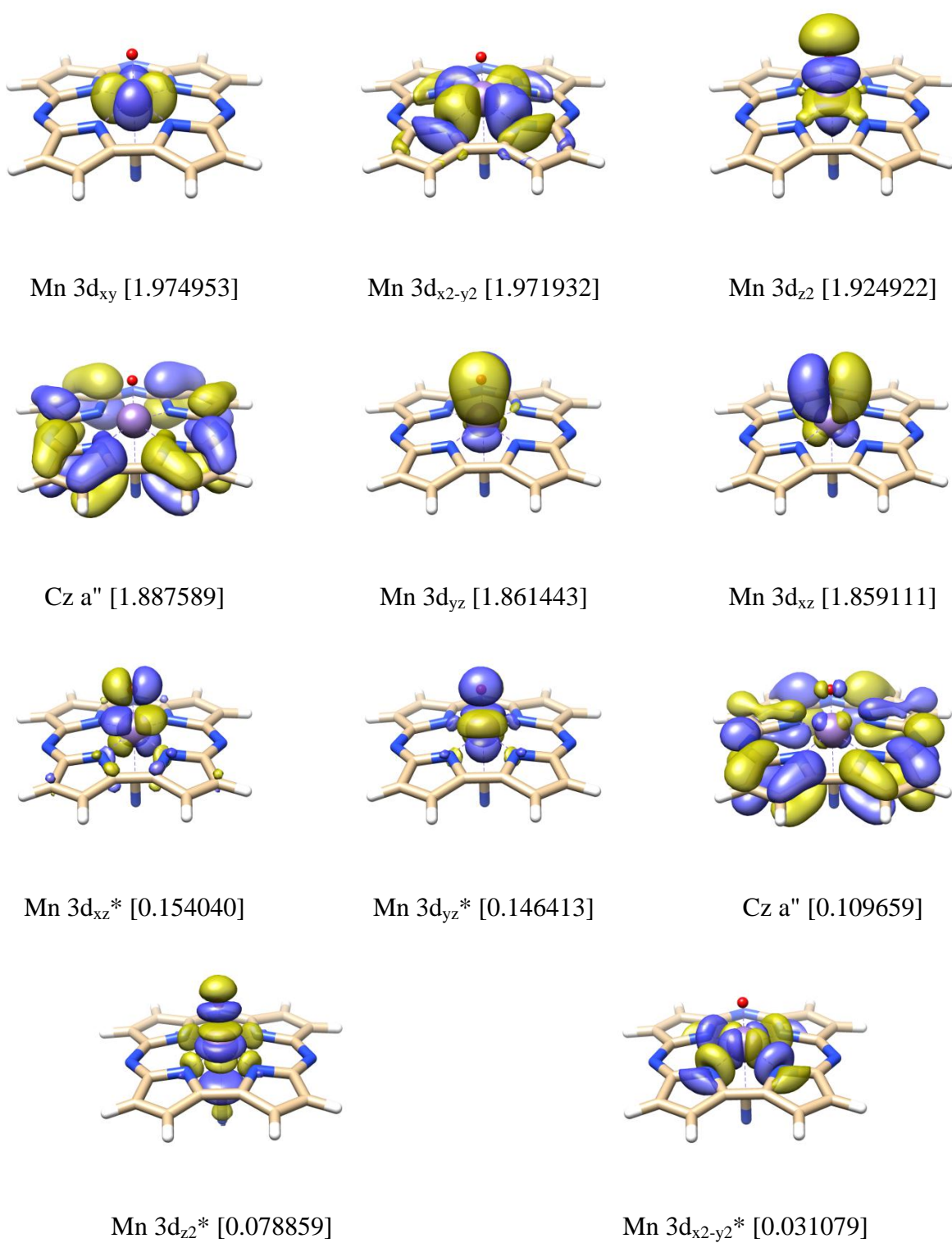
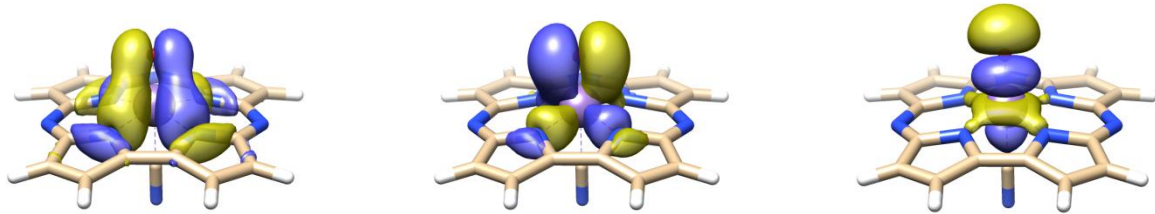


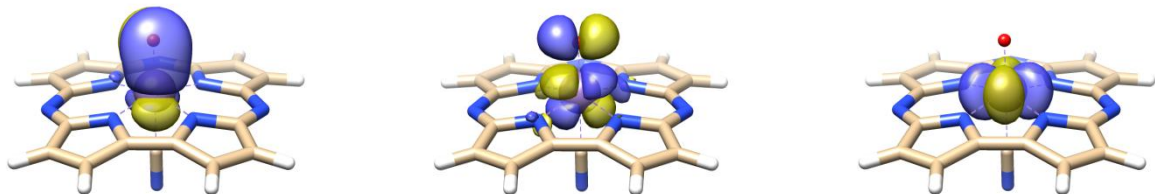
**Figure S13.** Active natural orbitals of  ${}^1[({\text{H}}_8{\text{Cz}}){\text{Mn}}(\text{O})(\text{CN})]^-$  from RIJCOSX-CASSCF(12,11)/cc-pVTZ/cc-pVDZ. The opposite phases are shown in either blue or yellow.



Mn  $3d_{x^2-y^2}+3d_{xz}$  [1.961049]

Mn  $3d_{x^2-y^2}-3d_{xz}$  [1.954375]

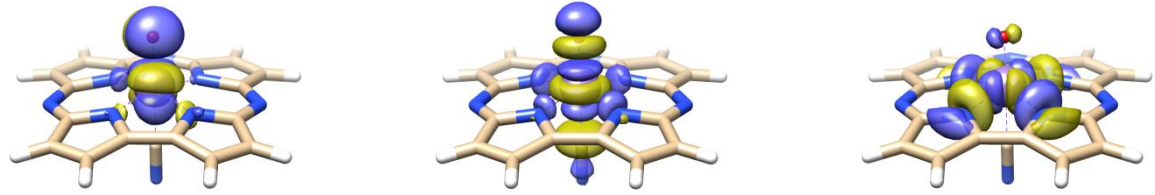
Mn  $3d_{z^2}$  [1.914916]



Mn  $3d_{yz}$  [1.767005]

Mn  $3d_{xz}^*$  [1.038674]

Mn  $3d_{xy}$  [0.999520]



Mn  $3d_{yz}^*$  [0.235718]

Mn  $3d_{z^2}^*$  [0.084931]

Mn  $d_{x^2-y^2}^*$  [0.043813]

**Figure S14.** Active natural orbitals of  ${}^3[({H_8Cz})Mn(O)(CN)]^-$  from RIJCOSX-CASSCF(10,9)/cc-pVTZ/cc-pVDZ using the optimized geometry of  ${}^1[({H_8Cz})Mn(O)(CN)]^-$ . The opposite phases are shown in either blue or yellow.

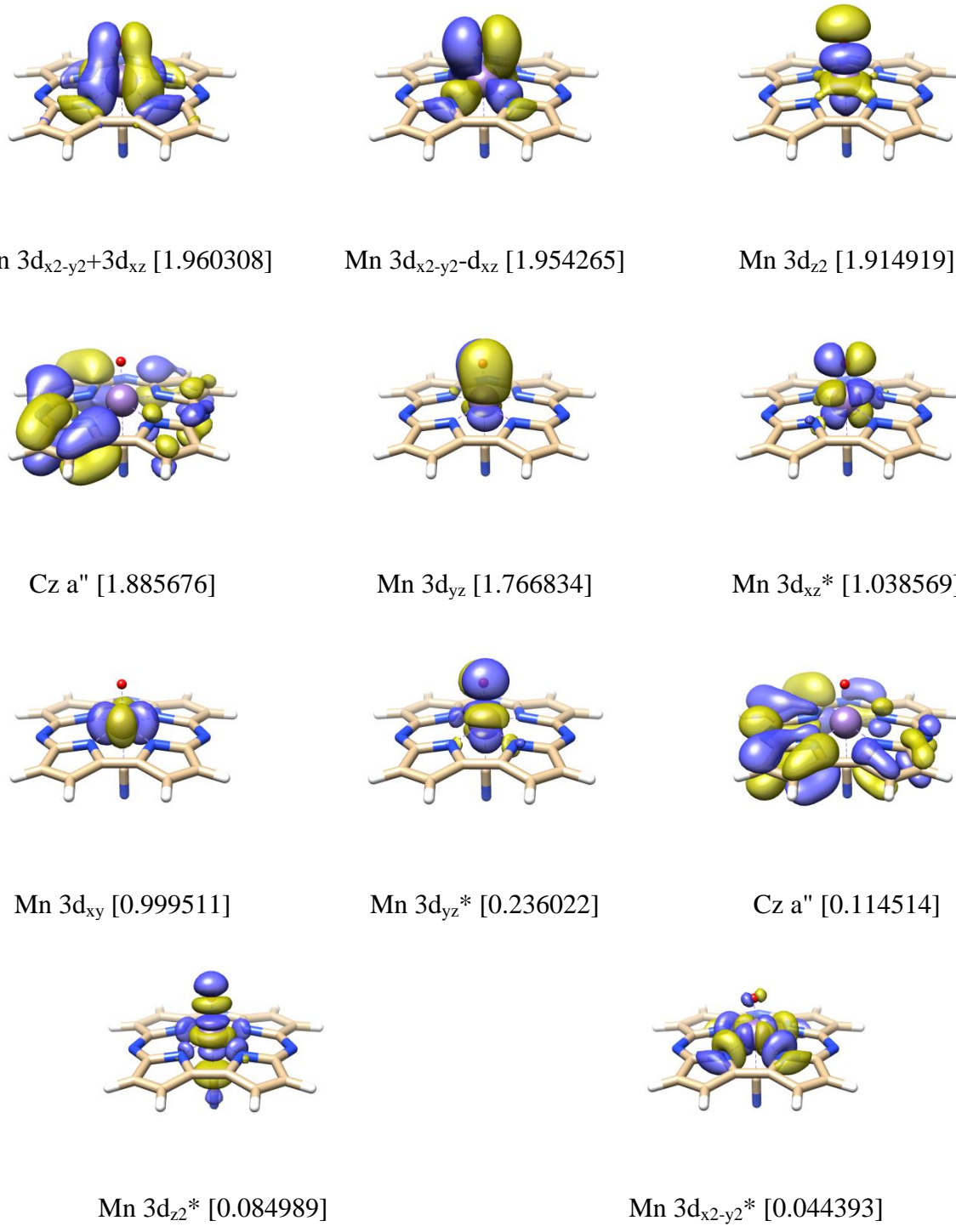


**Figure S15.** Active natural orbitals of  ${}^3[({\text{H}}_8{\text{Cz}}){\text{Mn}}(\text{O})(\text{CN})]^-$  from RIJCOSX-CASSCF(12,11)/cc-pVTZ/cc-pVDZ using the optimized geometry of  ${}^1[({\text{H}}_8{\text{Cz}}){\text{Mn}}(\text{O})(\text{CN})]^-$ . The opposite phases are shown in either blue or yellow.

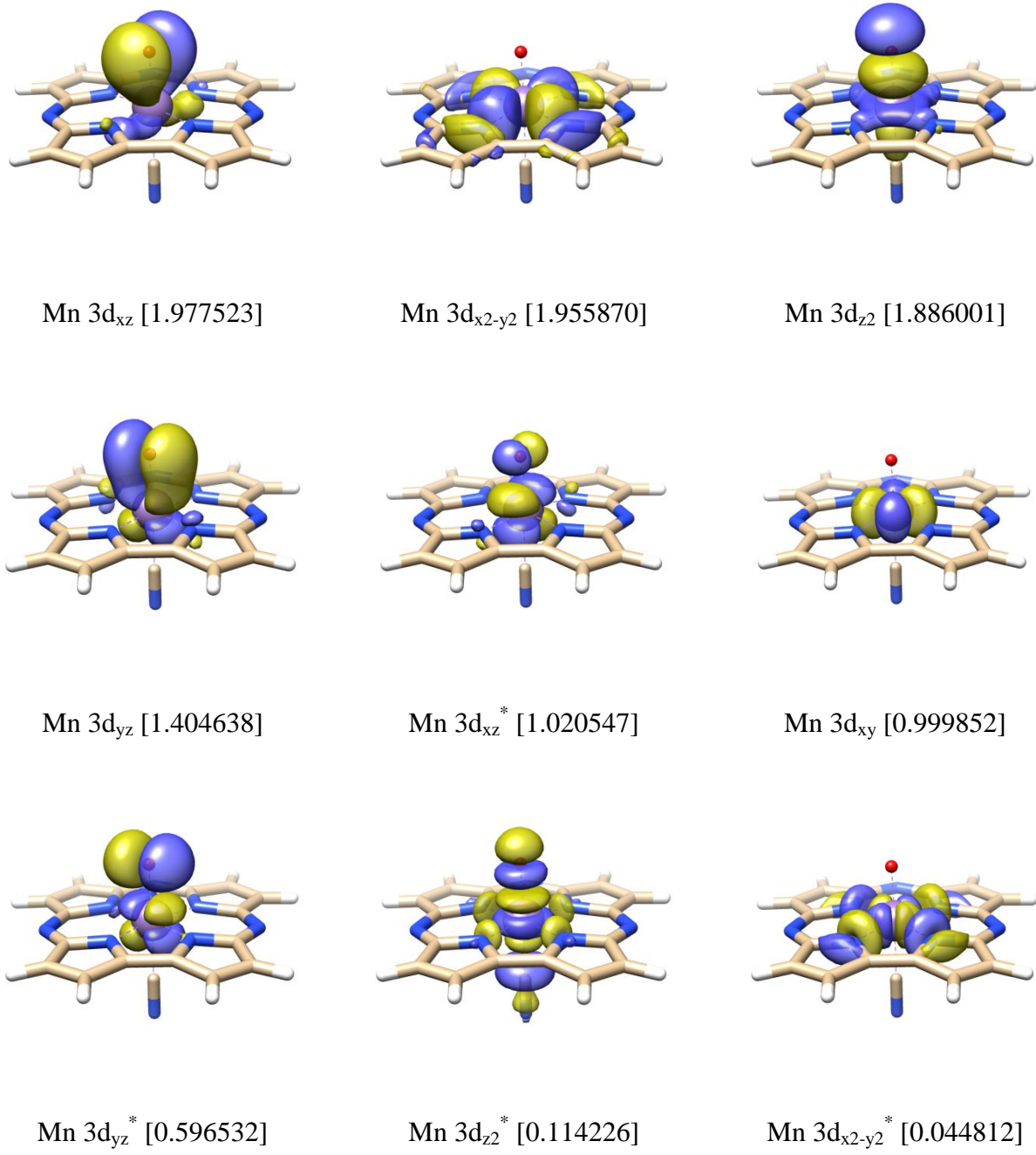


**Figure S16.** Active natural orbitals of  ${}^3[({\text{H}}_8{\text{Cz}}){\text{Mn}}(\text{O})(\text{CN})]^-$  from RIJCOSX-CASSCF(10,9)/cc-pVTZ/cc-pVDZ using the optimized geometry of  ${}^3[({\text{H}}_8{\text{Cz}}){\text{Mn}}(\text{O})(\text{CN})]^-$ . The opposite phases are shown in either blue or yellow.

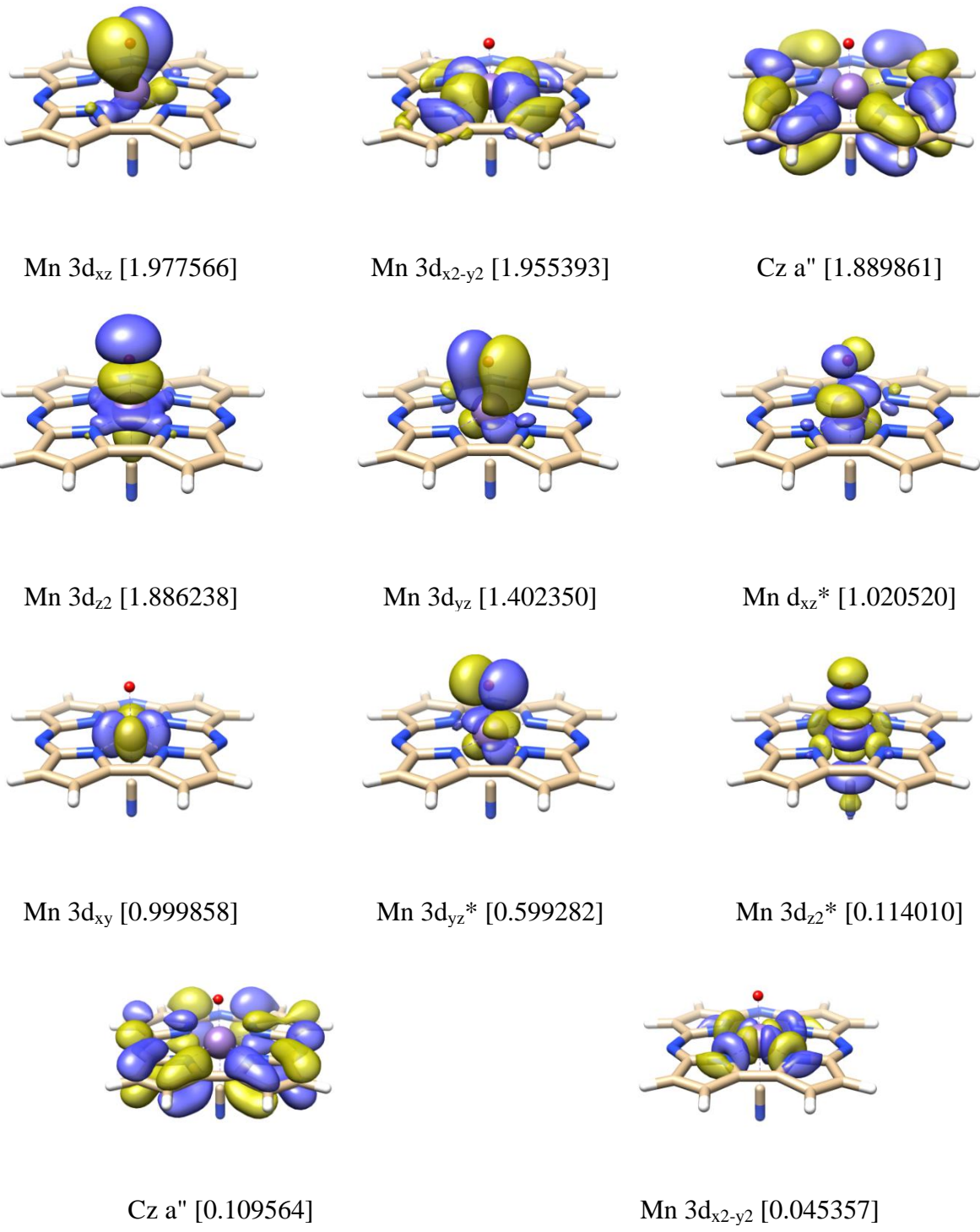


**Figure S17.** Active natural orbitals of  ${}^3[({\text{H}}_8{\text{Cz}}){\text{Mn}}(\text{O})(\text{CN})]^-$  from RIJCOSX-CASSCF(12,11)/cc-pVTZ/cc-pVDZ using the optimized geometry of  ${}^3[({\text{H}}_8{\text{Cz}}){\text{Mn}}(\text{O})(\text{CN})]^-$ . The opposite phases are shown in either blue or yellow.

**Table S18.** Configuration state functions with weight larger than 1.00% for  $^1[(\text{H}_8\text{Cz})\text{Mn}(\text{O})(\text{CN})]^-$  from RIJCOSX-CASSCF(10,9)/cc-pVTZ/cc-VDZ

Configuration	CSF	Weight (%)
1	222220000	81.75
2	222111100	3.14
3	222202000	2.63
4	222020200	2.53
5	221211010	1.80
6	221120110	1.75

**Table S19.** Configuration state functions with weight larger than 1.00% for  $^1[(\text{H}_8\text{Cz})\text{Mn}(\text{O})(\text{CN})]^-$  from RIJCOSX-CASSCF(12,11)/cc-pVTZ/cc-VDZ

Configuration	CSF	Weight (%)
1	22222200000	77.12
2	22202200200	3.87
3	22221111000	2.82
4	22220202000	2.37
5	22222020000	2.28
6	22121201010	1.65
7	22122110010	1.61

**Table S20.** Configuration state functions with weight larger than 1.00% for  $^3[(\text{H}_8\text{Cz})\text{Mn}(\text{O})(\text{CN})]^-$  from RIJCOSX-CASSCF(10,9)/cc-pVTZ/cc-VDZ using the optimized geometry of  $^1[(\text{H}_8\text{Cz})\text{Mn}(\text{O})(\text{CN})]^-$ .

Configuration	CSF	Weight (%)
1	222211000	78.71
2	222011200	5.68
3	222111100	4.08
4	221111110	2.42
5	212121100	1.39

**Table S21.** Configuration state functions with weight larger than 1.00% for  $^3[(\text{H}_8\text{Cz})\text{Mn}(\text{O})(\text{CN})]^-$  from RIJCOSX-CASSCF(12,11)/cc-pVTZ/cc-VDZ using the optimized geometry of  $^1[(\text{H}_8\text{Cz})\text{Mn}(\text{O})(\text{CN})]^-$ .

Configuration	CSF	Weight (%)
1	22222110000	74.14
2	22220112000	5.65
3	22202110200	4.42
4	22221111000	3.84
5	22121111010	2.27
6	21221211000	1.28

**Table S22.** Configuration state functions with weight larger than 1.00% for  ${}^3[({\text{H}_8\text{Cz}})\text{Mn}(\text{O})(\text{CN})]^-$  from RIJCOSX-CASSCF(10,9)/cc-pVTZ/cc-VDZ using the optimized geometry of  ${}^3[({\text{H}_8\text{Cz}})\text{Mn}(\text{O})(\text{CN})]^-$ .

Configuration	CSF	Weight (%)
1	222211000	54.20
2	222111100	18.36
3	222011200	15.88
4	221111110	2.18
5	220211020	1.14
6	221211010	1.04

**Table S23.** Configuration state functions with weight larger than 1.00% for  ${}^3[({\text{H}_8\text{Cz}})\text{Mn}(\text{O})(\text{CN})]^-$  from RIJCOSX-CASSCF(12,11)/cc-pVTZ/cc-VDZ using the optimized geometry of  ${}^3[({\text{H}_8\text{Cz}})\text{Mn}(\text{O})(\text{CN})]^-$ .

Configuration	CSF	Weight (%)
1	22222110000	51.02
2	22221111000	17.42
3	22220112000	15.04
4	22022110020	2.83
5	22211111100	2.04
6	22202110200	1.06

**Table S24.** Group spin densities of  ${}^1[({\text{H}_8\text{Cz}})\text{Mn}(\text{O})(\text{CN})]^-$ ,  ${}^3[({\text{H}_8\text{Cz}})\text{Mn}(\text{O})(\text{CN})]^-$  with singlet optimized geometry, and  ${}^3[({\text{H}_8\text{Cz}})\text{Mn}(\text{O})(\text{CN})]^-$  with triplet optimized geometry from RIJCOSX-CASSCF/cc-pVTZ/cc-VDZ with active space of (10,9) or (12,11)

Spin state	Geometry	Active Space	$\rho_{\text{Mn}}$	$\rho_{\text{O}}$	$\rho_{\text{C}_z}$	$\rho_{\text{CN}}$
0	Singlet	(10,9)	0.00	0.00	0.00	0.00
0	Singlet	(12,11)	0.00	0.00	0.00	0.00
1	Singlet	(10,9)	2.11	-0.09	-0.02	0.00
1	Singlet	(12,11)	2.11	-0.09	-0.02	0.00
1	Triplet	(10,9)	2.52	-0.47	-0.05	0.00
1	Triplet	(12,11)	2.52	-0.47	-0.04	0.00

**Table S25.** Absolute energies (in au) and relative energies (in kcal mol<sup>-1</sup> with respect to the singlet spin state of the same size of active space) of <sup>1</sup>[(H<sub>8</sub>Cz)Mn(O)(CN)]<sup>-</sup>, <sup>3</sup>[(H<sub>8</sub>Cz)Mn(O)(CN)]<sup>-</sup> with singlet optimized geometry, and <sup>3</sup>[(H<sub>8</sub>Cz)Mn(O)(CN)]<sup>-</sup> with triplet optimized geometry from RIJCOSX-CASSCF/cc-pVTZ/cc-VDZ with active space of (10,9) or (12,11)

Spin state	Geometry	Active Space	E	ΔE
0	Singlet	(10,9)	-2321.09	0.00
1	Singlet	(10,9)	-2321.08	5.55
1	Triplet	(10,9)	-2321.08	1.38
0	Singlet	(12,11)	-2321.10	0.00
1	Singlet	(12,11)	-2321.09	4.66
1	Triplet	(12,11)	-2321.09	1.30

**Table S26.** Absolute energies (in au) and relative energies (in kcal mol<sup>-1</sup> with respect to the singlet spin state of the same size of active space) of <sup>1</sup>[(H<sub>8</sub>Cz)Mn(O)(CN)]<sup>-</sup>, <sup>3</sup>[(H<sub>8</sub>Cz)Mn(O)(CN)]<sup>-</sup> with singlet optimized geometry, and <sup>3</sup>[(H<sub>8</sub>Cz)Mn(O)(CN)]<sup>-</sup> with triplet optimized geometry from RIJCOSX-RI-NEVPT2/cc-pVTZ/cc-VDZ with active space of (10,9) or (12,11)

Spin state	Geometry	Active Space	E	ΔE
0	Singlet	(10,9)	-2325.47	0.00
1	Singlet	(10,9)	-2325.45	12.82
1	Triplet	(10,9)	-2325.45	13.44
0	Singlet	(12,11)	-2325.46	0.00
1	Singlet	(12,11)	-2325.43	16.21
1	Triplet	(12,11)	-2325.44	12.51











































